Relative importance of poroelastic effects and viscoelastic relaxation for postseismic velocity fields after normal and thrust earthquakes: Insights from 2D finite-element modelling

Jill Peikert [a],[*], Andrea Hampel [a], Meike Bagge [b]

[a] *Institut für Geologie, Leibniz Universität Hannover, Callinstr. 30, 30167 Hannover, Germany*
[b] *GFZ German Research Centre for Geosciences, Telegrafenberg, 14473 Potsdam, Germany*

ABSTRACT

Earthquakes on faults in the brittle upper crust evoke sudden changes in pore fluid pressure as well as postseismic viscoelastic flow in the lower crust and lithospheric mantle but the relative importance of these processes during the postseismic phase has not been systematically studied. Here, we use two-dimensional finite-element models to investigate how pore fluid pressure changes and postseismic viscoelastic relaxation interact during the earthquake cycle of an intracontinental dip-slip fault. To isolate the effects from pore fluid flow and viscoelastic relaxation from each other, we performed experiments with and without pore fluid flow and viscoelastic relaxation, respectively. In different experiments, we further varied the permeability of the crust and the viscosity of lower crust or lithospheric mantle. Our model results show poroelastic effects dominate the velocity field in the first months after the earthquake. In models considering poroelastic effects, the surfaces of both hanging wall and footwall of the normal fault subside at different velocities, while they move upwards in the thrust fault model. Depending on the permeability and viscosity values, viscoelastic relaxation dominates the velocity field from about the second postseismic year onward although poroelastic effects may still occur if the permeability of the upper crust is sufficiently low. With respect to the spatial scales of poroelastic effects and viscoelastic relaxation, our results show that pore fluid pressure changes affect the velocity field mostly within 10–20 km around the fault, whereas the signal from viscoelastic relaxation is recognizable up to several tens of kilometres away from the fault. Our findings reveal that both poroelastic effects and viscoelastic relaxation may overlap earlier and over longer time periods than previously thought, which should be considered when interpreting aftershock distributions, postseismic Coulomb stress changes and surface displacements.

1. Introduction

A fault ruptured by an earthquake experiences sudden coseismic slip and a stress drop. On the surrounding region, the earthquake has several effects. First, the sudden coseismic slip alters the pore pressure in the fluid-saturated crust (e.g. King and Muir-Wood, 1994; Nur and Booker, 1972; Sibson, 1994). These earthquake-induced poroelastic effects can lead to considerable pore fluid pressure gradients, which are subsequently relaxed in the postseismic phase by fluid flow from overpressurized to under-pressurized regions given sufficient permeability (e.g. Antonioli et al., 2005; Chiarabba et al., 2009). The magnitude of the pore pressure change and the duration of the postseismic fluid migration depend on the elastic and hydraulic properties of the crust

(Biot, 1941; Rice and Cleary, 1976). Poroelastic effects are typically strongest within 1–2 fault lengths around the source fault and act on timescales of days to a few years after the earthquake (Albano et al., 2017; Antonioli et al., 2005; Chiarabba et al., 2009; Tung and Masterlark, 2018). High pore fluid pressure gradients and the resulting postseismic pore fluid migration may trigger aftershocks by reducing the normal stress (Chiarabba et al., 2009; Malagnini et al., 2012; Nur and Booker, 1972). Second, the coseismic fault movement, which usually occurs in the brittle upper crust, causes a sudden stress increase below the brittle-ductile transition (e.g. Ellis and Stöckhert, 2004). This stress that is coseismically imposed on the lower crust and lithospheric mantle is relaxed by viscoelastic flow, a process called postseismic relaxation (Nur and Mavko, 1974). Postseismic viscoelastic relaxation in the lower

crust and/or lithospheric mantle typically acts on local to regional spatial scales and on timescales of years to decades depending on the viscosity of the lithospheric layers (Freed and Lin, 1998; Gourmelen and Amelung, 2005; Hampel and Hetzel, 2015; Kenner and Segall, 1999; Masterlark and Wang, 2002; Pollitz, 1997).

Both pore fluid pressure changes and viscoelastic relaxation affect the stress and velocity fields in the crust (Barbot and Fialko, 2010). After major earthquakes, geodetic data provide information on the co- and postseismic surface deformation, which is then often used for calculating Coulomb stress changes induced on other faults in the region of the earthquake (e.g. Serpelloni et al., 2012). Based on the assumption that the spatial and temporal scales of the two processes are sufficiently different, analyses of geodetic data or Coulomb stress changes often neglect either pore fluid pressure changes (Freed and Lin, 2001; Luo and Liu, 2010) or viscoelastic relaxation (e.g. Albano et al., 2017, 2019, 2021; Nespoli et al., 2018). Only few studies considered the contributions of both processes to surface deformation and Coulomb stress changes after a major intracontinental earthquake (e.g. Masterlark and Wang, 2002; Ryder et al., 2007, 2010; Tung and Masterlark, 2018). With respect to the relative importance of poroelastic effects and viscoelastic relaxation, the studies came to different conclusions. While Tung and Masterlark (2018) argue that poroelastic effects were the primary trigger of the Visso earthquake following the 2016 Amatrice earthquake, Ryder et al. (2007, 2010) observed a prevalence of the viscoelastic relaxation signal in the interferometric synthetic aperture radar (InSAR) data from the 1997 Manyi and 2008 Nima-Gaize (Tibet) earthquakes. This suggest that viscoelastic relaxation may be important already during the early postseismic phase, as indicated also by the results from numerical models (Hampel and Hetzel, 2015). However, these earlier models did not include poroelasticity.

In this study, we investigate the relative importance of the poroelastic effects and postseismic viscoelastic relaxation during the earthquake cycle of an intracontinental normal or thrust fault. To achieve this, we use two-dimensional finite element models, which include gravity, pore fluid pressure, viscoelastic lithospheric layers and interseismic strain accumulation. By varying the permeability of the crust and the viscosity of the lithospheric layers in different experiments, we investigate the spatial and temporal evolution of poroelastic effects and viscoelastic relaxation in terms of co- and postseismic pore pressure changes as well as postseismic vertical and horizontal velocities. Our model results show that poroelastic effects and postseismic viscoelastic relaxation may overlap already in the early postseismic phase, with the consequence that the velocity field in the crust shows a combined signal of both processes. Our findings have important implications for the

analysis of geodetic records of earthquakes and for the calculation of postseismic Coulomb stress changes.

2. Model setup and conducted experiments

2.1. Model setup

The two-dimensional finite-element models in this study are generated by the commercial software ABAQUS (version 2018). The models represent a 500-km-wide and 100-km-thick section of the lithosphere, which is divided into a 15-km-thick elastic upper crust, a 15-km-thick viscoelastic lower crust and a 70-km-thick viscoelastic lithospheric mantle (Fig. 1). The general setup of the reference models with a 60°-dipping normal fault or 30°-dipping thrust fault and the rheological parameters of the layers (Poisson's ratio ν, viscosity η, density ρ, Young's modulus E) are shown in Fig. 1. The model fault is embedded in the model centre in the upper crust as a frictional contact interface between the footwall and the hanging wall (friction coefficient μ). The contact is implemented as surface-to-surface contact (cf. ABAQUS Documentation, 2018), i.e. slip on the fault occurs by relative movement between the element surfaces of footwall and hanging wall. Whether slip on the model fault can occur during the model run, is controlled by the boundary conditions for the fault, which can be changed between locked (= no slip allowed) and unlocked (= slip is allowed) (cf. ABAQUS Documentation, 2018). When the model fault is unlocked, slip initiation is controlled by the Mohr-Coulomb criterion $|\tau_{max}| = c + \mu \, \sigma_n$, where τ_{max} is the critical shear stress, c is the cohesion (zero in our model), σ_n is the normal stress and μ is the coefficient of friction. The sense of slip, i.e. normal or reverse, is controlled by either extending or shortening of the model domain, respectively, which is achieved by applying a velocity boundary condition to the model sides (Fig. 1).

Viscoelastic behaviour is implemented as linear, temperature-independent Maxwell viscoelasticity. To simulate the coupling between solid and fluid phase, we apply the coupled pore fluid diffusion/ stress analysis in ABAQUS, which requires – besides the Young's modulus and Poisson ratio of the solid phase – the permeability, the void ratio and the saturation as input parameters. The permeability K enters ABAQUS as the hydraulic conductivity k_f that can be calculated from k_f = K * ρ_{fluid} * g / η_{fluid} (ρ_{fluid}: fluid density, 1000 kg/m^3; acceleration due to gravity, 9.81 m/s^2; η_{fluid}: fluid viscosity, 998 × 10^{-6} kg m^{-1} s^{-1}). The void ratio is defined as the proportion between the volume of voids and solids in the medium and the volume of fluid trapped in the medium. The void ratio typically is a few per cent for crystalline basement rocks (cf. Masterlark and Wang, 2002; Masterlark, 2003). In our models, we
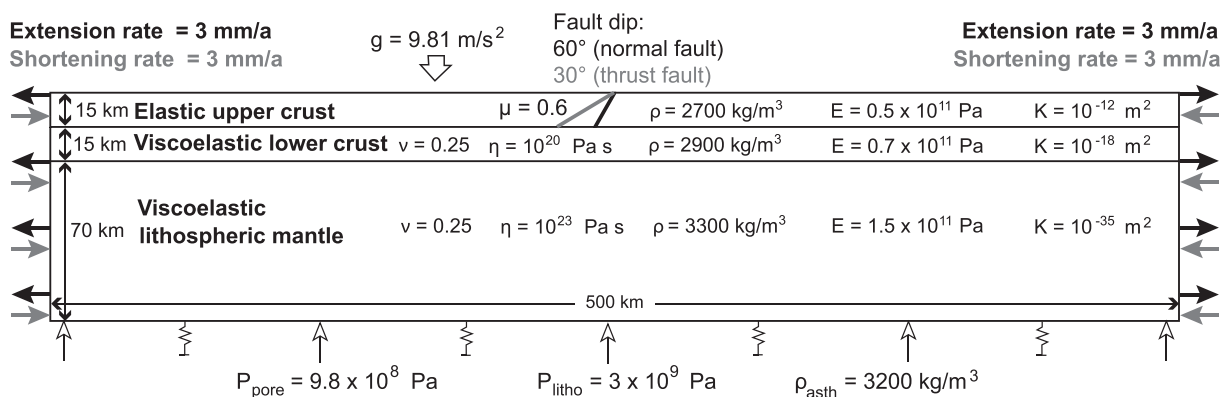

Fig. 1. Setup of the two-dimensional finite-element reference models (R1$_{nf}$, R1$_{tf}$) with a 60°-dipping normal fault or a 30°-dipping thrust fault. The lithosphere is subdivided into an elastic upper crust, viscoelastic lower crust and viscoelastic lithospheric mantle. The fault (friction coefficient μ) is embedded in the upper crust. Material properties are density (ρ), Young's modulus (E), Poisson's ratio (ν), viscosity (η) and permeability (K). Viscosity and permeability are varied in different experiments. Gravity is included as a body force. A lithostatic pressure and an elastic foundation, which represent the asthenosphere, are applied to the model bottom to implement isostatic effects (cf. Hampel et al., 2019). The model bottom is free to move in the vertical and horizontal directions; the model sides are free to move in the vertical direction. At the model sides a velocity boundary condition is applied to extend or shorten the model at a total rate of 6 mm/a.

use a void ratio of 0.06 and a saturation of 1. The fault is treated as impermeable, i.e. fluid cannot flow across it (cf. Albano et al., 2017, 2019; Dempsey et al., 2013; Rudnicki, 1986). This is supported by observations from natural faults as well as by results from experiments, which show that faults act as a barrier to fluid flow once an impermeable fault gouge layer has developed (Ingebritsen and Manning, 2010; Parsons et al., 1999; Piombo et al., 2005; Scholz, 1987). Moreover, no pore fluid flow will occur across the model boundaries. The initial pore pressure (P_{pore}) distribution in the models is hydrostatic. Gravity is included as a body force in all models, as well as isostatic effects, which are simulated by applying a lithostatic pressure (P_{litho}) of 3×10^9 Pa and an elastic foundation to the model bottom (marked as arrows and springs in Fig. 1) (cf. Hampel et al., 2019). The property of the elastic foundation represents an asthenosphere with a density of 3200 kg/m^3. The stiffness of the elastic foundation is calculated from the product of density of the asthenosphere ρ_{asth} and gravitational acceleration g. As initial condition, a lithostatic stress field is defined. All models are meshed by second-order rectangular elements with an average edge length of ~1 km.

Each model run consists of three model phases (Table 1) (cf. Bagge and Hampel, 2016, 2017; Hampel and Hetzel, 2012, 2015; Hampel et al., 2013). Viscoelastic behaviour and pore fluid flow are activated during the first model phase and remain active until the end of each model run. During the first model phase, the frictional contact between the fault hanging wall and footwall, lithostatic and hydrostatic pressure distributions as well as a state of isostatic equilibrium are established in the model. The model fault is unlocked but slip, i.e. relative movement between footwall and hanging wall, is not yet initiated. The first model phase lasts 300 ka to ensure that pore fluid flow and viscoelastic deformation triggered solely by applying gravity has ceased before the next model phase. During the second model phase, the model is extended or shortened, which initiates slip on the fault. Once slip is initiated, the fault is allowed to continuously accumulate slip until it reaches a constant slip rate. Continuous fault slip at a constant slip rate simulates slip accumulation integrated over many earthquake cycles and ensures that the results obtained from the subsequent third model phase do not depend on the number of previous earthquake cycles (cf. Hampel and Hetzel, 2012, 2015; Hampel et al., 2013). The model time needed to achieve a constant slip rate depends primarily on the fault dip and the viscosity structure of the lithosphere (cf. Hampel et al., 2010). In the present study, the second model phase lasts ca. 250 ka in the normal fault model and 950 ka in the thrust fault, respectively. Extension or shortening continues through the third model phase, which comprises the preseismic, coseismic and postseismic phases. During the preseismic phase, during which the fault is locked, slip accumulation stops. The length of the preseismic phase is chosen such that the fault experiences 2 m of coseismic slip during subsequent coseismic phase. Depending on the slip rate of the fault, the length of the preseismic phase varies between ca. 3800 and 4200 a in the different experiments. At the

Table 1
Overview of model phases.

Model phase	Description	Applied model components	State of fault
1	Establishment of contact along fault and of isostatic and hydrostatic equilibrium	Gravity, isostasy, pore fluid flow, viscoelastic material behaviour	Unlocked (but slip not yet initiated)
2	Extension or shortening of model domain until fault reaches constant slip rate	Gravity, isostasy, pore fluid flow, viscoelastic material behaviour, extension/shortening	Unlocked (continuous slip)
3	Preseismic phase	Gravity, isostasy, pore fluid flow,	Locked
	Coseismic phase	viscoelastic material behaviour,	Unlocked
	Postseismic phase	extension/shortening	Locked

beginning of the coseismic phase (30 s), the fault is switched from locked to unlocked, which causes sudden slip on the fault. The slip distribution is not prescribed but develops freely. The size of the earthquake is controlled by the applied far-field extension or shortening rate, the rheological properties of the model, and the duration of the preseismic phase. In this study, we define the duration of the preseismic phase such that the maximum coseismic slip is 2 m, which would be the typical slip of an $M_w \sim 7$ intraplate earthquake if we assume a fault length of 40 km (Wells and Coppersmith, 1994). During the postseismic phase (50 model years), we lock the fault again while extension or shortening continues to simulate the interseismic deformation and the related stress increase. Note that potential afterslip is not considered because our intention is to evaluate the effects from pore fluid pressure changes and viscoelastic relaxation.

2.2. Conducted experiments

To investigate the relative importance of poroelastic effects and postseismic viscoelastic relaxation during the coseismic and postseismic phases, we conducted the following experiments. First, we computed normal and thrust fault reference models ($R1_{nf}$, $R1_{tf}$), in which we used permeability values and a viscosity structure typical of continental lithosphere (Fig. 1, Table 2) (Chen and Molnar, 1983; Ingebritsen and Manning, 2010; Klemperer, 2006; Manning and Ingebritsen, 1999; Ryder et al., 2014; Shi et al., 2015; Stober and Bucher, 2015). To isolate the effect of pore fluid flow and viscoelastic relaxation, we performed additional runs of the reference models, in which we switched off either viscoelastic behaviour ($R2_{nf}$, $R2_{tf}$) or pore fluid flow ($R3_{nf}$, $R3_{tf}$) during the postseismic phase. Second, we computed models, in which we varied the permeability of the crust from 10^{-11} to 10^{-17} m^2 for the upper crust and 10^{-17} to 10^{-19} m^2 for the lower crust while keeping the viscosity structure constant ($P1-6_{nf}$, $P1-6_{tf}$, Table 2) (Ingebritsen and Manning, 2010; Manning and Ingebritsen, 1999; Stober and Bucher, 2015). For the lithospheric mantle, we apply a permeability of $K = 10^{-35}$ m^2, which represents an impermeable layer (Tung et al., 2018a). Third, we ran experiments, in which we varied the viscosity for the lower crust and lithospheric mantle between 10^{19} and 10^{22} Pa s and between 10^{22} and 10^{23} Pa s, respectively ($V1-3_{nf}$, $V1-3_{tf}$, Table 2). These values represent the range of viscosities derived for continental lithosphere (Burov and Watts, 2006; England et al., 2013; Gourmelen and Amelung, 2005; Henriquet et al., 2019; Kaufmann and Amelung, 2000; Klemperer, 2006; Nishimura and Thatcher, 2003). Fourth, we calculated selected end-member model configurations, in which we varied both permeability and viscosity values ($PV1-4_{nf}$, $PV1-4_{tf}$, Table 2).

3. Results

In the following, we first show the results from the normal and thrust fault reference models for the coseismic (Section 3.1) and postseismic phase (Section 3.2.1). In Sections 3.2.2 to 3.2.4, we present the postseismic velocity fields and pore pressure distributions from the models, in which we varied the permeability of the crust and/or the viscosity of the lower crust or lithospheric mantle (Table 2).

3.1. Coseismic phase

Fig. 2 illustrates the coseismic vertical and horizontal displacement fields as well as the coseismic pore pressure changes, as obtained from the normal and thrust fault reference models ($R1_{nf}$, $R1_{tf}$). The sudden slip on the model fault causes footwall uplift and hanging wall subsidence in the normal fault model and hanging wall uplift and footwall subsidence in the thrust fault model (Fig. 2a, b). In the normal fault model, horizontal surface displacements are directed away from the fault (Fig. 2c, d), indicating extension across the fault. Within the fault footwall, shortening prevails, while alternating zones of extension and shortening occur within the hanging wall (Fig. 2e) (cf. Hampel and

Table 2
Overview of numerical models of this study.

Model name[a]	Permeability of upper crust K_{uc} (m^2)	Permeability of lower crust K_{lc} (m^2)	Viscosity of lower crust η_{lc} (Pa s)	Viscosity of lithospheric mantle η_{lm} (Pa s)	Results shown in figure(s)
Reference models					
R1$_{nf}$, R1$_{tf}$	10^{-12}	10^{-18}	10^{20}	10^{23}	2–5
R2$_{nf}$, R2$_{tf}$	10^{-12}	10^{-18}	–	–	3–5
R3$_{nf}$, R3$_{tf}$	–	–	10^{20}	10^{23}	3–5
Models with variable permeability					
P1$_{nf}$, P1$_{tf}$	10^{-11}	10^{-18}	10^{20}	10^{23}	6a, S1a
P2$_{nf}$, P2$_{tf}$	10^{-13}	10^{-18}	10^{20}	10^{23}	6b, S1b
P3$_{nf}$, P3$_{tf}$	10^{-15}	10^{-18}	10^{20}	10^{23}	7a, S2a
P4$_{nf}$, P4$_{tf}$	10^{-17}	10^{-18}	10^{20}	10^{23}	7b, S2b
P5$_{nf}$, P5$_{tf}$	10^{-12}	10^{-17}	10^{20}	10^{23}	S3a, S4a
P6$_{nf}$, P6$_{tf}$	10^{-12}	10^{-19}	10^{20}	10^{23}	S3b, S4b
Models with variable viscosity					
V1$_{nf}$, V1$_{tf}$	10^{-12}	10^{-18}	10^{19}	10^{23}	8a, S5a
V2$_{nf}$, V2$_{tf}$	10^{-12}	10^{-18}	10^{22}	10^{23}	8b, S5b
V3$_{nf}$, V3$_{tf}$	10^{-12}	10^{-18}	10^{20}	10^{22}	S6
Endmember models with variable permeability and viscosity					
PV1$_{nf}$, PV1$_{tf}$	10^{-11}	10^{-18}	10^{19}	10^{23}	9a, S7a
PV2$_{nf}$, PV2$_{tf}$	10^{-17}	10^{-18}	10^{19}	10^{23}	9b, S7b
PV3$_{nf}$, PV3$_{tf}$	10^{-11}	10^{-18}	10^{22}	10^{23}	10a, S8a
PV4$_{nf}$, PV4$_{tf}$	10^{-17}	10^{-18}	10^{22}	10^{23}	10b, S8b

[a] Subscripts nf and tf refer to normal fault and thrust fault, respectively.

Hetzel, 2015; see Section 4.1 for discussion). In the thrust fault model, horizontal movements indicate coseismic shortening across the fault, while footwall and hanging wall experience extension (Fig. 2d, e). For comparison, vertical and horizontal displacements obtained from analytical solutions for an elastic half-space (Okada, 1985) are shown as dashed lines in Fig. 2b and d (cf. Beauducel, 2022) (see Section 4.1 for discussion).

Coseismic pore pressure changes occur mainly in the lower part of the fault and reach highest positive or negative values around the fault tip with a radius of 1–2 km (Fig. 2f). In the normal fault reference model, the coseismic slip leads to an over-pressurization of the hanging wall (~11 MPa) and an under-pressurization of the footwall by ~10 MPa with respect to the hydrostatic pressure. In contrast, the pore pressure decreases by ~5 MPa in the thrust fault hanging wall and increases by ~6 MPa in the footwall relative to the hydrostatic values. The zone of negative pore pressure changes in the thrust fault hanging wall expands from the fault tip to the surface of the model.

3.2. Postseismic phase

3.2.1. Reference models

In this section, we analyse the postseismic vertical and horizontal velocity fields derived from the reference models (R1$_{nf}$, R1$_{tf}$) together with the results from the model runs without viscoelastic behaviour (R2$_{nf}$, R2$_{tf}$) or without pore fluid flow (R3$_{nf}$, R3$_{tf}$), respectively (Figs. 3, 4). Afterwards, we present the postseismic pore pressure evolution at different time intervals in the normal and thrust fault reference models with and without viscoelastic relaxation (Fig. 5). To account for the generally non-linear evolution of the postseismic deformation, the model results are shown at irregular time intervals, i.e. for model stages between which the largest changes occur. In general, these are the first months and years after the earthquake.

Fig. 3 shows the evolution of the vertical and horizontal velocity fields derived from the normal fault reference models (R1$_{nf}$, R2$_{nf}$, R3$_{nf}$). In the reference model R1$_{nf}$ (Fig. 3a), high vertical and horizontal velocities with absolute values ranging from ca. -1400 to 700 mm/a occur in the upper crust in the first month after the earthquake. Notably, the model surface subsides on both sides of the fault. Horizontal movements of the hanging wall and footwall are directed toward the fault. In the second month after the earthquake, the principal patterns of the velocity fields are similar to the first month, but the vertical and horizontal

velocities decrease to −70 and 10 mm/a and − 45 and 30 mm/a, respectively. From the third month onwards, the velocities further decrease. The hanging wall shows subsidence at a rate of −4 mm/a near the surface while the footwall is uplifted at the fault tip by the same rate. The horizontal movements of the hanging wall and footwall change direction, with the highest velocities occurring in the hanging wall near the fault. The velocity patterns integrated over the first year largely reflect the patterns observed in the early stage of the year (see Section 4.1 for discussion). In the following years, higher vertical velocities only occur within a few kilometres around the fault and slightly decrease over the next 50 years. The horizontal velocities also decrease over time but remain elevated up to distances of ~60 km compared to the undisturbed velocity field.

The model without viscoelastic behaviour (R2$_{nf}$, Fig. 3b) shows the same velocity patterns in the early postseismic phase as the reference model R1$_{nf}$, but from the third month onwards, perturbations of both vertical and horizontal velocities become weaker. The vertical velocity field shows hanging wall subsidence (−3 mm/a) in the third month after the earthquake, which largely disappears in the following month, and slight footwall uplift near the fault tip (0.7 mm/a) in the following 50 years appears. From the sixth month onwards, the horizontal velocity field is dominated by the regional extension. In contrast to models R1$_{nf}$ and R2$_{nf}$, the model without pore fluid flow (R3$_{nf}$, Fig. 3c) shows footwall uplift and hanging wall subsidence at maximum rates of 3 and − 4 mm/a, respectively, near the fault tip from the first month onwards. The horizontal velocity field shows extension across the fault and velocity perturbations at distances of up to 60 km with highest velocities of 3 mm/a near the fault tip. Over the entire period, the vertical and horizontal velocity patterns remain similar, with a gradual decrease in the velocities over the next 50 years.

The thrust fault reference model R1$_{tf}$ (Fig. 4a) shows high vertical and horizontal velocities ranging from −400 to 2000 mm/a and from −900 to 900 mm/a, respectively, in the first month after the earthquake. On both sides of the fault, the model surface is uplifted. The horizontal movements of the hanging wall and footwall are directed away from the fault. Over the next months, the velocity patterns change, with the footwall starting to subside and the horizontal movements changing to shortening across the fault. Similar to the normal fault reference model R1$_{nf}$, the velocity patterns of the first year are dominated by the high velocities of the early postseismic phase. From the second year onwards, the hanging wall is uplifted and the footwall subsides at rates of up to 1
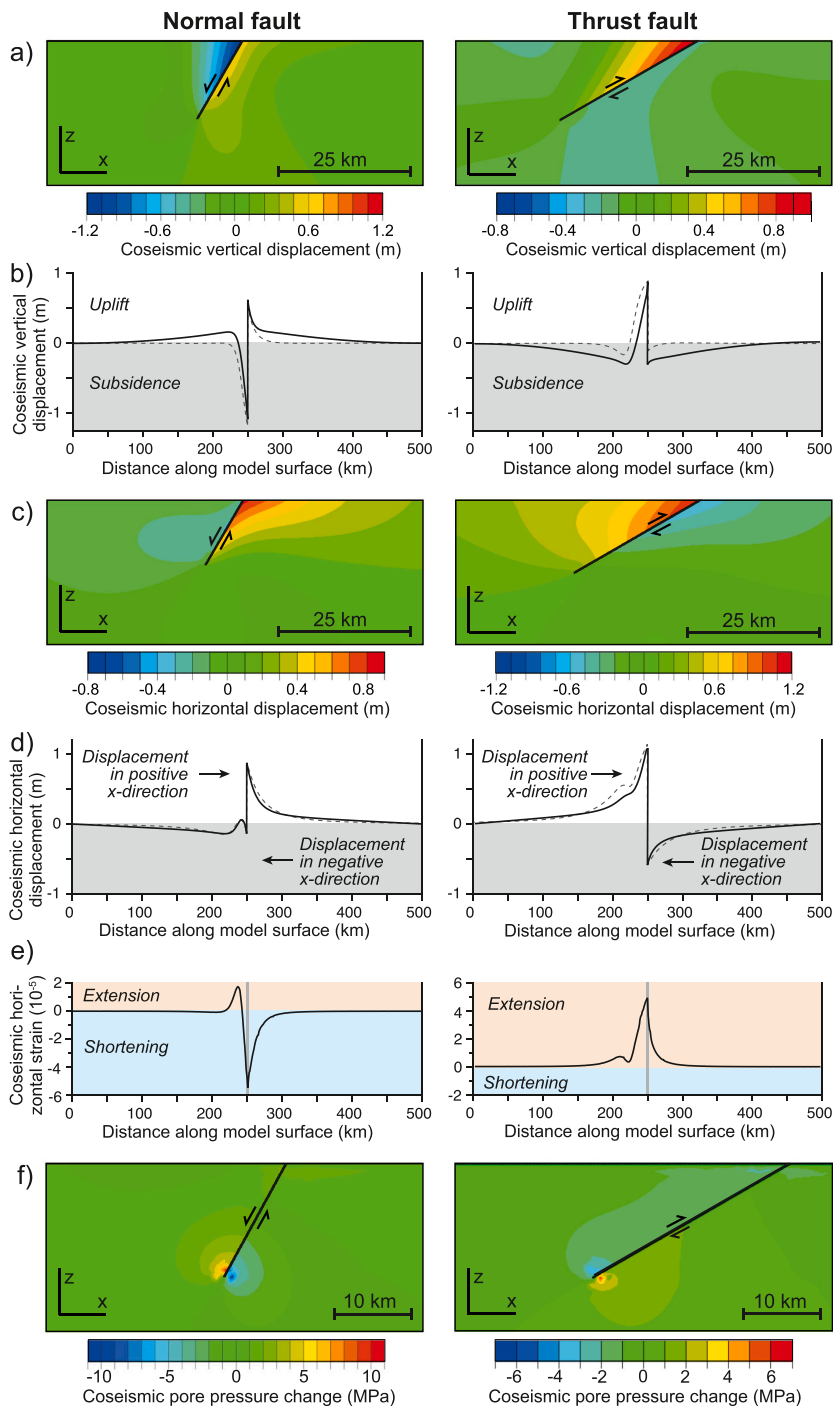
Fig. 2. Model results for the coseismic phase in the normal fault reference model (left column) and thrust fault reference model (right column). a) Vertical displacement field around the fault. b) Vertical displacement for a profile along the model surface. c) Horizontal displacement field around the fault. b) Horizontal displacement for a profile along the model surface. e) Horizontal strain for a profile along the model surface. f) Pore pressure changes with respect to hydrostatic values. Model sections around the fault in figure parts a, c and f are shown without vertical exaggeration. Dashed lines in figure parts b and d represent curves based on the analytical solution (Okada, 1985; Beauducel, 2022).

and − 2 mm/a, respectively. The largest horizontal velocity perturbations occur around the fault tip and in a > 50 km wide zone in the footwall and hanging wall. The velocities slightly decrease over the period of 50 years after the earthquake.

The thrust fault model without viscoelastic behaviour (R2$_{tf}$, Fig. 4b) shows the same velocity patterns in the early postseismic stage as model R1$_{tf}$. In the third month, the velocity fields are still disturbed near the fault, but these perturbations dissipate over the next few years. After the second year, the velocity field induced by the regional shortening dominates. In the model without pore fluid flow (R3$_{tf}$; Fig. 4c), the vertical and horizontal velocity fields are disturbed up to several kilometres away from the fault, with highest velocities occurring near the fault tip (3 mm/a) from the first month onwards. In contrast to models

R1$_{tf}$ and R2$_{tf}$, which show uplift on both sides of the fault, model R3$_{tf}$ shows hanging wall uplift and footwall subsidence. The velocity patterns of model R3$_{tf}$ remain similar over the 50 years after the earthquake, with only negligible velocity changes.

The postseismic evolution of the pore pressure in the normal and thrust fault reference models with and without viscoelastic relaxation (R1$_{nf}$, R2$_{nf}$, R1$_{tf}$, R2$_{tf}$) is illustrated in Fig. 5. A comparison with the coseismic phase (Fig. 2) shows that the pore pressure changes are inverted relative to the coseismic distribution, i.e. zones with previously positive values now exhibit negative values and vice versa. In the first month, the magnitudes of the pore pressure changes are almost equivalent to the ones in the coseismic phase (i.e. ±11 MPa in the normal fault model R1$_{nf}$ and ±6 MPa in the thrust fault model R1$_{tf}$), which implies
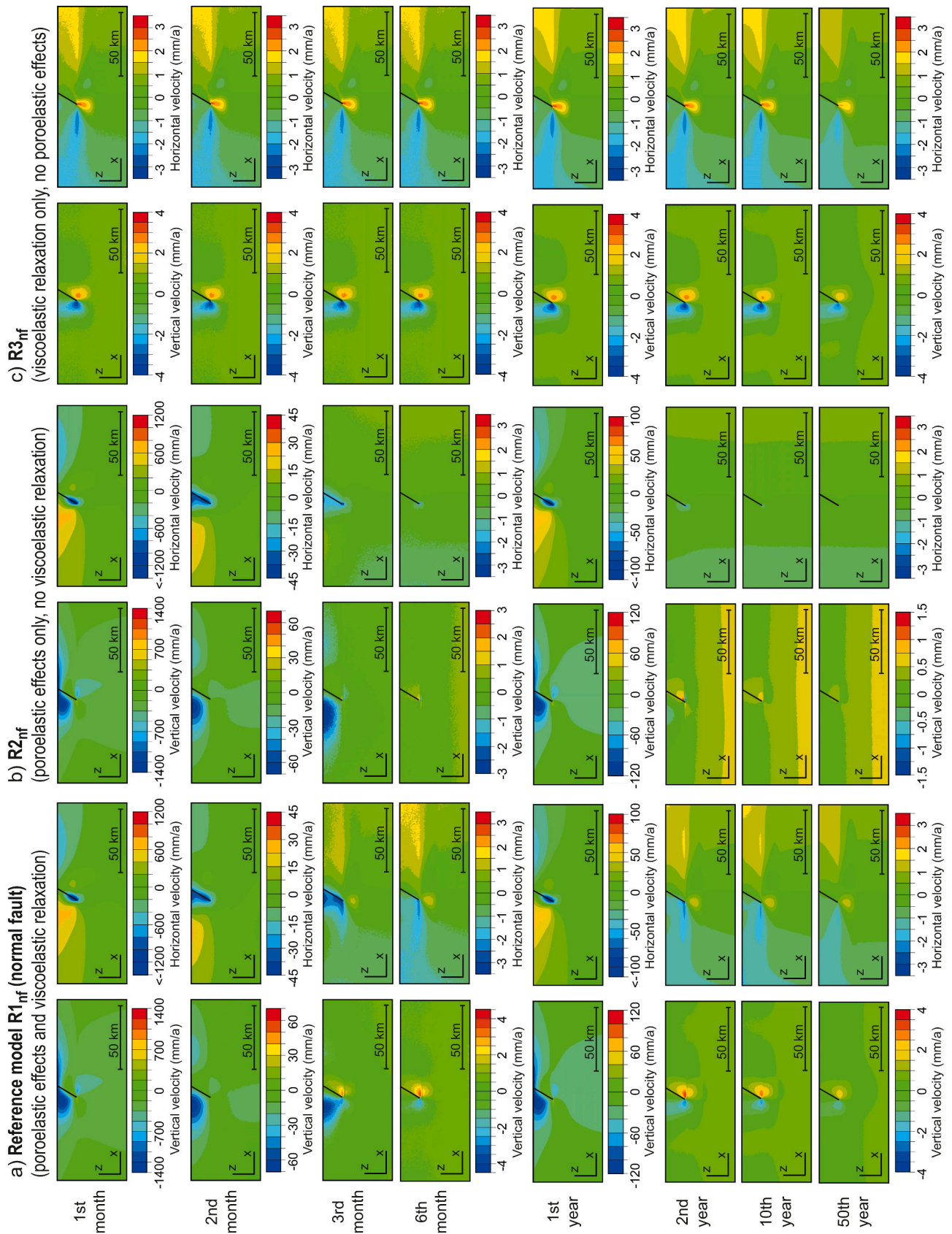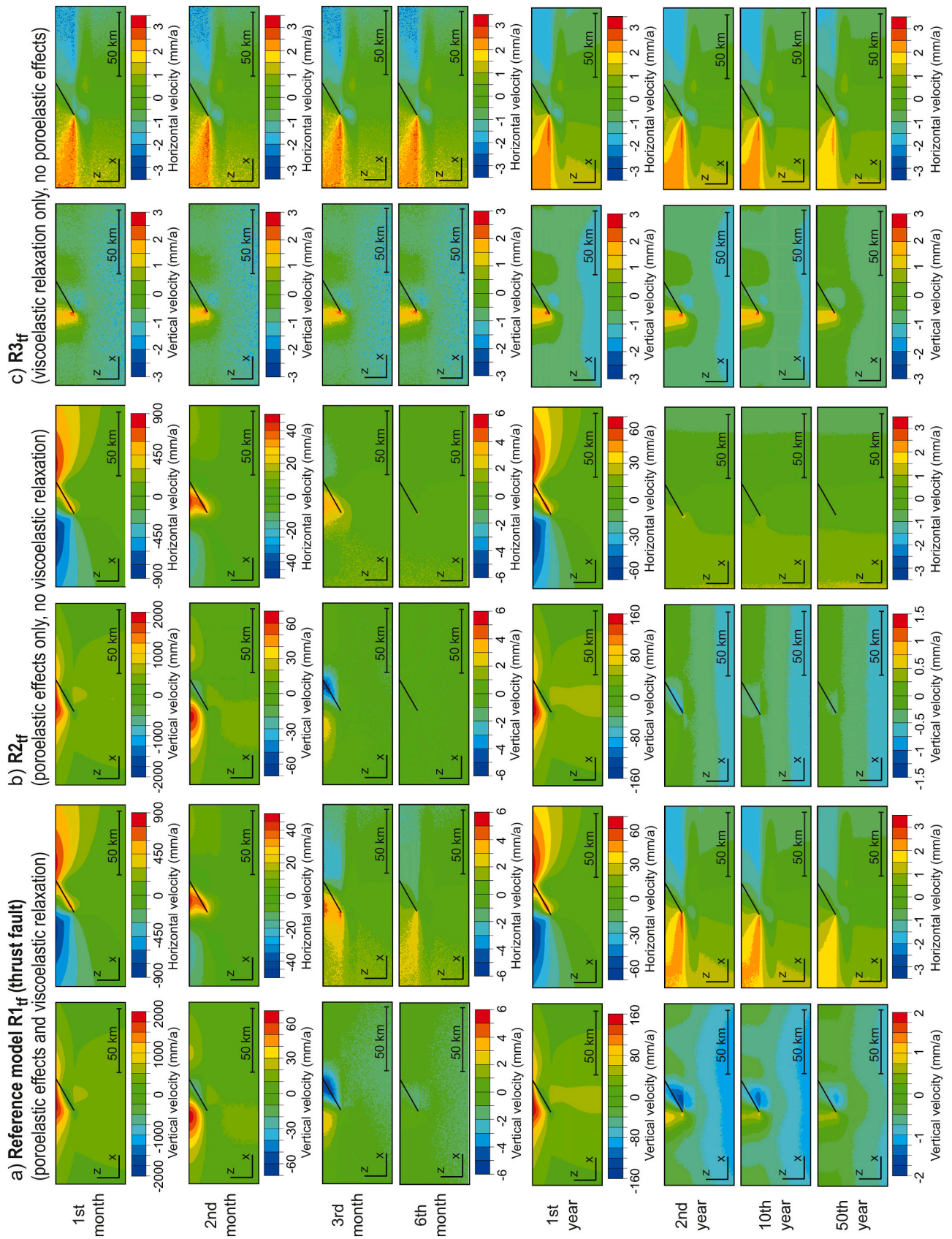
Fig. 3. Postseismic velocity fields from the normal fault reference model (a) R1$_{nf}$ (with both poroelastic and viscoelastic effects), (b) R2$_{nf}$ (poroelastic effects, no viscoelastic relaxation) and (c) R3$_{nf}$ (viscoelastic relaxation, no poroelastic effects). Shown is a section in the model centre around the fault (no vertical exaggeration). Note that the velocity fields at all time points are averaged over the respective time interval, i.e. the velocity field for the first postseismic year is integrated over the time period between the beginning and the end of the first year after the earthquake.

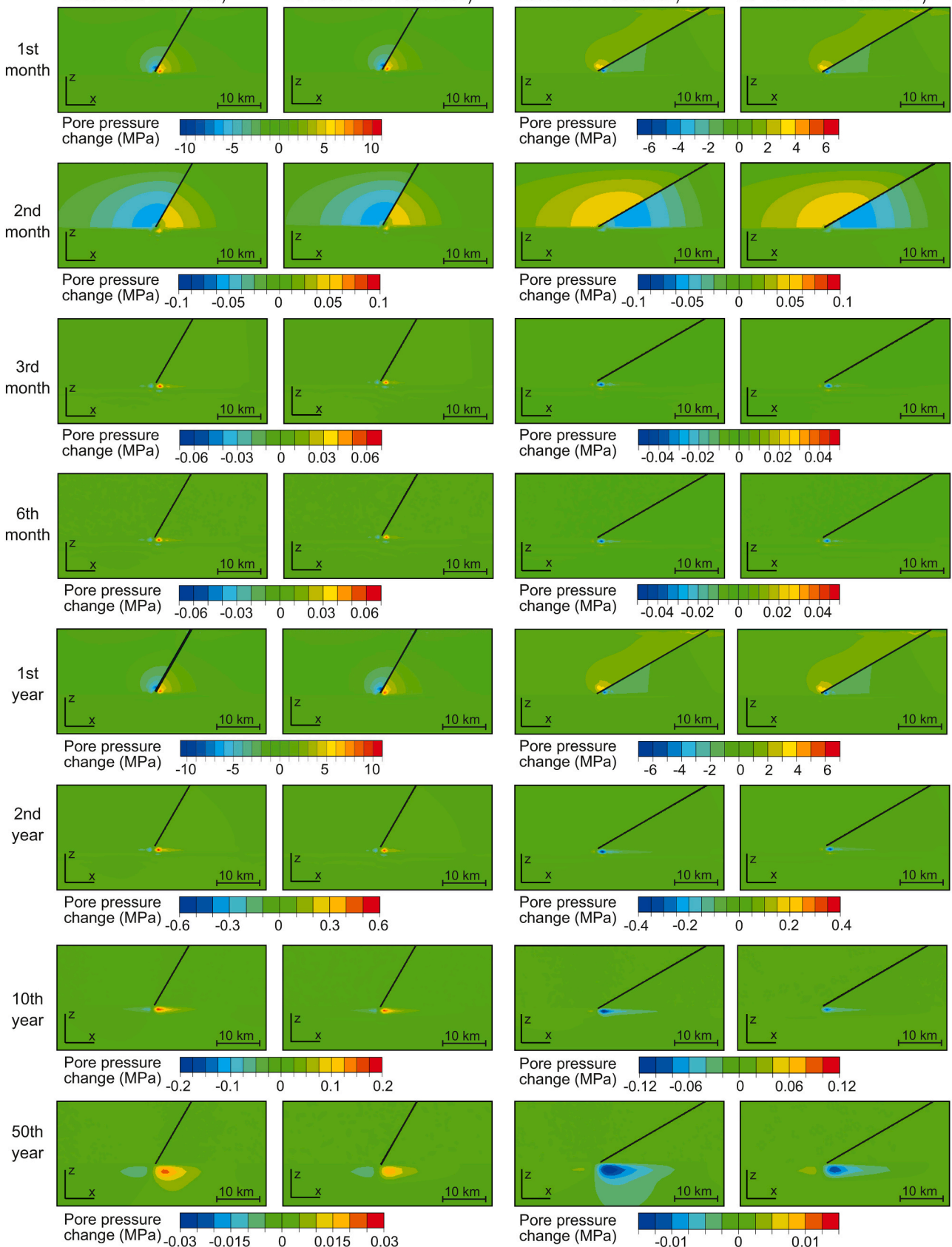**Fig. 4.** Postseismic velocity fields from the thrust fault reference model (a) R1$_{tf}$ (with both poroelastic and viscoelastic effects), (b) R2$_{tf}$ (poroelastic effects, no viscoelastic relaxation) and (c) R3$_{tf}$ (viscoelastic relaxation, no poroelastic effects). Shown is a section in the model centre around the fault. No vertical exaggeration. Note that the velocity fields at all time points are averaged over the respective time interval, i.e. the velocity field for the first postseismic year is integrated over the time period between the beginning and the end of the first year after the earthquake.

(caption on next page)

Fig. 5. Postseismic pore pressure changes with respect to hydrostatic values for (a) the normal fault reference model R1$_{nf}$ and (b) the thrust fault reference model R1$_{tf}$ and for the reference models without viscoelastic relaxation (R2$_{nf}$, R2$_{tf}$). Shown is a section in the model centre around the fault (no vertical exaggeration). Note that the pore pressure changes at all time points are averaged over the respective time interval, i.e. the pore pressure change for the first postseismic year is integrated over the time period between the beginning and the end of the first year after the earthquake. Reference models R3$_{nf}$ and R3$_{tf}$ are not shown here as they do not consider pore pressure effects.

that the coseismically induced pore pressure changes have largely dissipated. In other words, the hydrostatic pore pressure distribution is almost recovered in both models already in the early postseismic phase. In the second month, the pore pressure changes decrease rapidly by two orders of magnitude and expand within the upper crust toward the surface because of the fluid diffusion. The pore pressure changes during the first year after the earthquake reflects the pore pressure pattern of the first month. Over the next 50 years, the values decrease by up to three orders of magnitude. Notable, while the pore pressure changes are concentrated around the fault during the first two years after the earthquake, zones of small positive and negative pore pressure changes develop in the lower crust beneath the fault during the late postseismic phase. Compared to the reference models R1$_{nf}$ and R1$_{tf}$ (left column of Fig. 5a and b), the models without viscoelastic relaxation (R2$_{nf}$, R2$_{tf}$) (right column of Fig. 5a and b) show a similar pore pressure evolution. Differences between the models occur mainly in the late postseismic phase, where the models without viscoelastic relaxation (R2$_{nf}$, R2$_{tf}$) show smaller zones with negative and positive pore pressure changes in the lower crust than the reference models R1$_{nf}$ and R1$_{tf}$.

3.2.2. Models with variable permeability

In this section, we show the results for selected normal and thrust fault models, in which we varied the permeability of the upper or lower crust while keeping the viscosity structure constant (Table 2; Figs. 6-7 and S1-S4). Compared to the reference models R1$_{nf}$ and R1$_{tf}$ the models with upper-crustal permeabilities of 10^{-11} m^2 (P1$_{nf}$, P1$_{tf}$) and 10^{-13} m^2 (P2$_{nf}$, P2$_{tf}$) show a similar evolution of the velocity fields over the time interval of 50 years, with some minor differences in the early post-seismic stage. These differences include slightly higher velocities during the first month in models P1$_{nf}$ and P1$_{tf}$ followed by a stronger decrease than in the reference models R1$_{nf}$ and R1$_{tf}$ (Fig. 6a, S1a), whereas models P2$_{nf}$ and P2$_{tf}$ show slightly lower initial postseismic velocities than the reference models (R1$_{nf}$, R1$_{tf}$) but velocities remain higher until the sixth month (Fig. 6b, S1b). Hydrostatic conditions in the pore fluid pressure changes are largely reached during the first month in the models P1$_{nf}$ and P1$_{tf}$ and during the second month in models P2$_{nf}$ and P2$_{tf}$.

For a permeability of 10^{-15} m^2 (P3$_{nf}$, P3$_{tf}$), the postseismic velocities are overall lower than in the reference models (R1$_{nf}$, R1$_{tf}$) and show a different evolution (Fig. 7a, S2a). In the first month and until the fifth year, the velocity fields are only perturbed around the fault tip and at the model surface on both sides of the fault, which show subsidence in the normal fault model (P3$_{nf}$) and uplift in the thrust fault model (P3$_{tf}$). The horizontal movements are directed toward the normal fault and away from the thrust fault, which persist until the second year after the earthquake. After the fifth year, the horizontal velocity field switches back to movements directed away from the normal fault and toward the thrust fault, respectively. With respect to the pore pressure changes, models P3$_{nf}$ and P3$_{tf}$ show a prolonged relaxation, i.e. in the first month, the pore pressure changes by only ±8 MPa in the normal fault model and by up to −5 MPa in the thrust fault model. The pore pressure expands within the upper crust toward the surface in the fifth year in both models (P3$_{nf}$, P3$_{tf}$). The migration of the pore pressure changes along the boundary between upper and lower crust and into the lower crust is recognizable in the tenth year in both models.

In the models with an upper-crustal permeability of 10^{-17} m^2 (P4$_{nf}$, P4$_{tf}$), the magnitudes of the vertical and horizontal velocities are one order lower during the first year after the earthquake than in the reference models R1$_{nf}$ and R1$_{tf}$ but the velocity decrease after this first

year occurs more gradually (Fig. 7b, S2b). Regarding the horizontal movements and the resulting shortening or extension, the velocity field evolution resembles those of models P3$_{nf}$ and P3$_{tf}$. The pore pressure changes decrease by up to ±4 MPa and ±3 MPa in the normal and thrust fault model, respectively. As a result, the coseismically induced pore pressure changes are not completely dissipated in the first year after the earthquake. Until the 50th year after the earthquake, the pore pressure changes decrease further and slowly expand around the fault tip.

Changes in the permeability of the lower crust have only minor influence on the postseismic velocity fields (Supplementary Figs. S3, S4). Compared to the reference models (R1$_{nf}$, R1$_{tf}$), a higher permeability of 10^{-17} m^2 (P5$_{nf}$, P5$_{tf}$) leads to a slower change of the velocity patterns after the second month (Fig. S3a, S4a). Up to the fifth year, velocities remain high in an area around the fault tip. Horizontal movements directed toward the normal fault (P5$_{nf}$) and away from the thrust fault (P5$_{tf}$) prevail already from the third month onwards. After the fifth year, the evolution of the velocity fields largely resembles the one of the reference models R1$_{nf}$ and R1$_{tf}$. Pore pressure changes in the models P5$_{nf}$ and P5$_{tf}$ are similar to the reference models (R1$_{nf}$, R1$_{tf}$) during the first month while they are higher around the fault tip until the second year. In the following years, the pore pressure changes migrate into the lower crust. Using a permeability of 10^{-19} m^2 for the lower crust (P6$_{nf}$, P6$_{tf}$) does not change the evolution of the velocity field over the entire model time of 50 years relative to the reference models R1$_{nf}$ and R1$_{tf}$ (Fig. S3b, S4b). The pattern of the pore pressure changes develops largely similarly to the reference models, however, the gradual decrease after the first month and from the first year onward as well as the magnitude and the extent of the pore pressure changes into the lower crust differ from the reference models (R1$_{nf}$, R1$_{tf}$).

3.2.3. Models with variable viscosity

In the next model series, we varied the viscosity of the lower crust or lithospheric mantle while keeping the permeability structure constant (Table 2; Figs. 8 and S5-S6). Generally, a change in viscosity affects the magnitudes but not the patterns of the postseismic velocities during the first year. The pore pressure changes are largely similar to the reference models R1$_{nf}$ and R1$_{tf}$ during the first postseismic year, with their magnitude being somewhat higher.

For a lower-crustal viscosity of 10^{19} Pa s (V1$_{nf}$, V1$_{tf}$), the maximum vertical and horizontal velocities during the third and sixth month are up to one magnitude higher than in the reference model R1$_{nf}$ and R1$_{tf}$ (Fig. 8a, S5a). In both models (V1$_{nf}$, V1$_{tf}$), the horizontal velocity field is highly disturbed around the fault tip but also >100 km away from the fault in both upper crust and upper part of the lower crust. In the 20th year, both models still show maximum velocities of 7–9 mm/a. Thus, a lower viscosity in the lower crust leads to higher velocities than in the reference models R1$_{nf}$ and R1$_{tf}$ until the 20th year. After 20 years, a new zone of subsidence (normal fault model V1$_{nf}$) and uplift (thrust fault model V1$_{tf}$) develops 50 km away from the fault. Below this zone, horizontal movements are directed toward the normal fault and away from the thrust fault, which is in contrast to the prevailing horizontal velocity fields induced by the regional deformation. With respect to the pore pressure, changes by ±12 MPa in the normal fault model (V1$_{nf}$) and ±6 MPa in the thrust fault model (V1$_{tf}$) can be observed in the first month, which decrease by up to two orders of magnitude in the following month and expand into the upper crust toward the surface. Hydrostatic conditions are largely reached after the second month. Until the end of the model runs, the pore pressure changes migrate into the lower crust and the magnitude decreases.
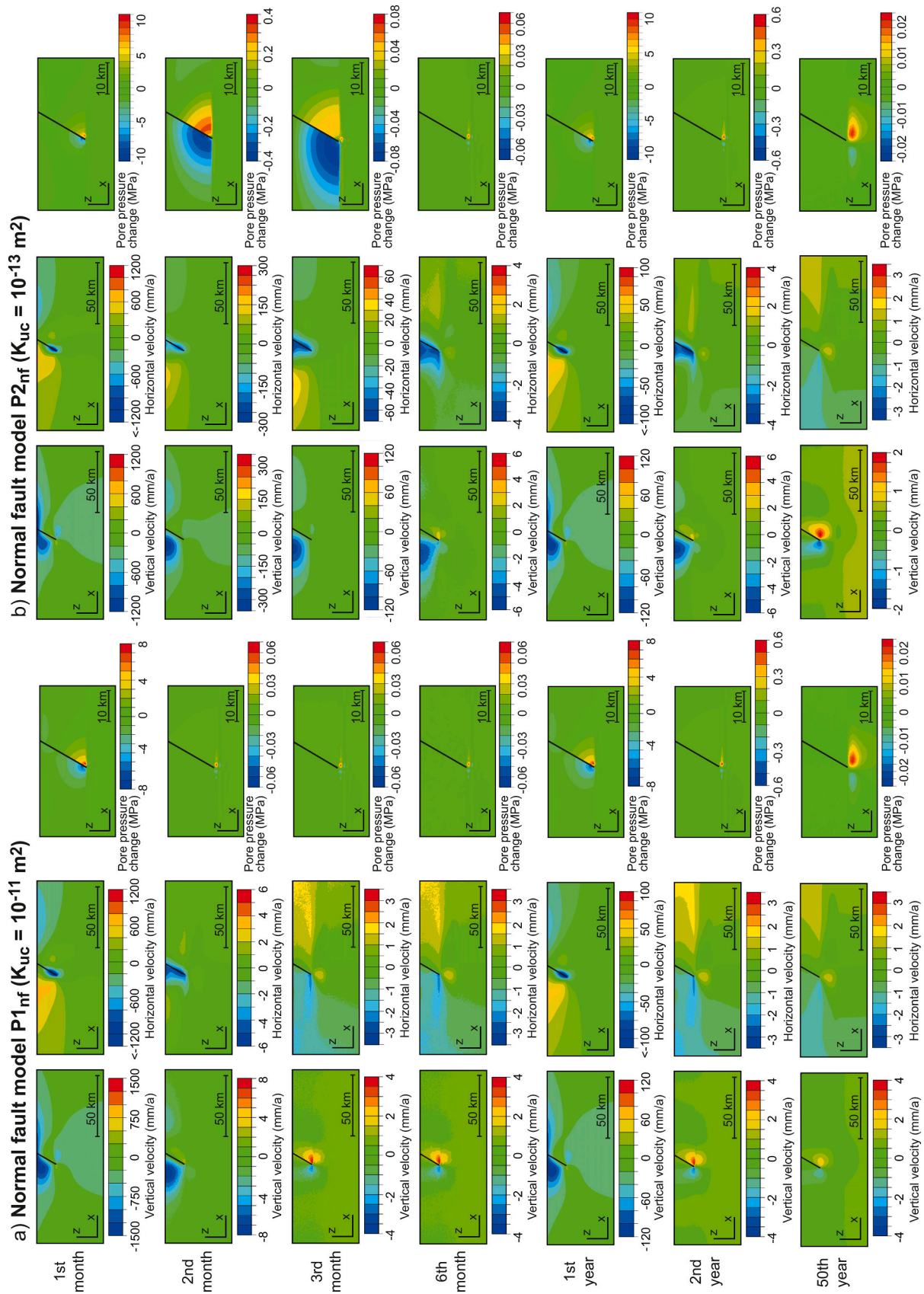
Fig. 6. Postseismic velocity fields and pore pressure changes from normal fault models (a) P1$_{nf}$ with an upper-crustal permeability of $K_{uc} = 10^{-11}$ m^2 and (b) P2$_{nf}$ with an upper-crustal permeability of $K_{uc} = 10^{-13}$ m^2. No vertical exaggeration. Note that the velocity fields and pore pressure changes at all time points are averaged over the respective time interval, i.e. the velocity field and pore pressure change for the first postseismic year is integrated over the time period between the beginning and the end of the first year after the earthquake.
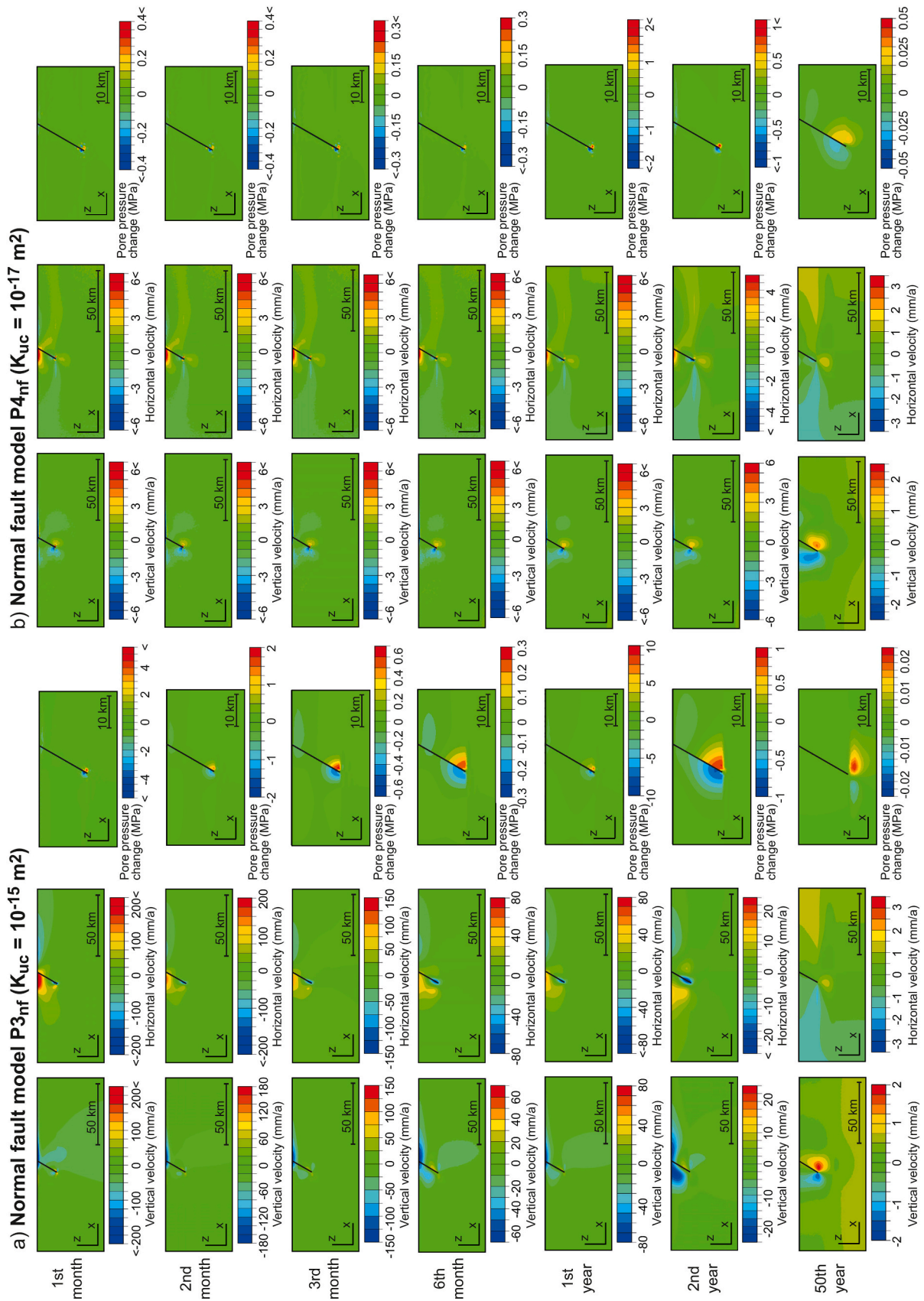
Fig. 7. Postseismic velocity fields and pore pressure changes from normal fault models (a) P3$_{nf}$ with an upper-crustal permeability of $K_{uc} = 10^{-15}$ m^2 and (b) P4$_{nf}$ with an upper-crustal permeability of $K_{uc} = 10^{-17}$ m^2. No vertical exaggeration. Note that the velocity fields and pore pressure changes at all time points are averaged over the respective time interval, i.e. the velocity field and pore pressure change for the first postseismic year is integrated over the time period between the beginning and the end of the first year after the earthquake.
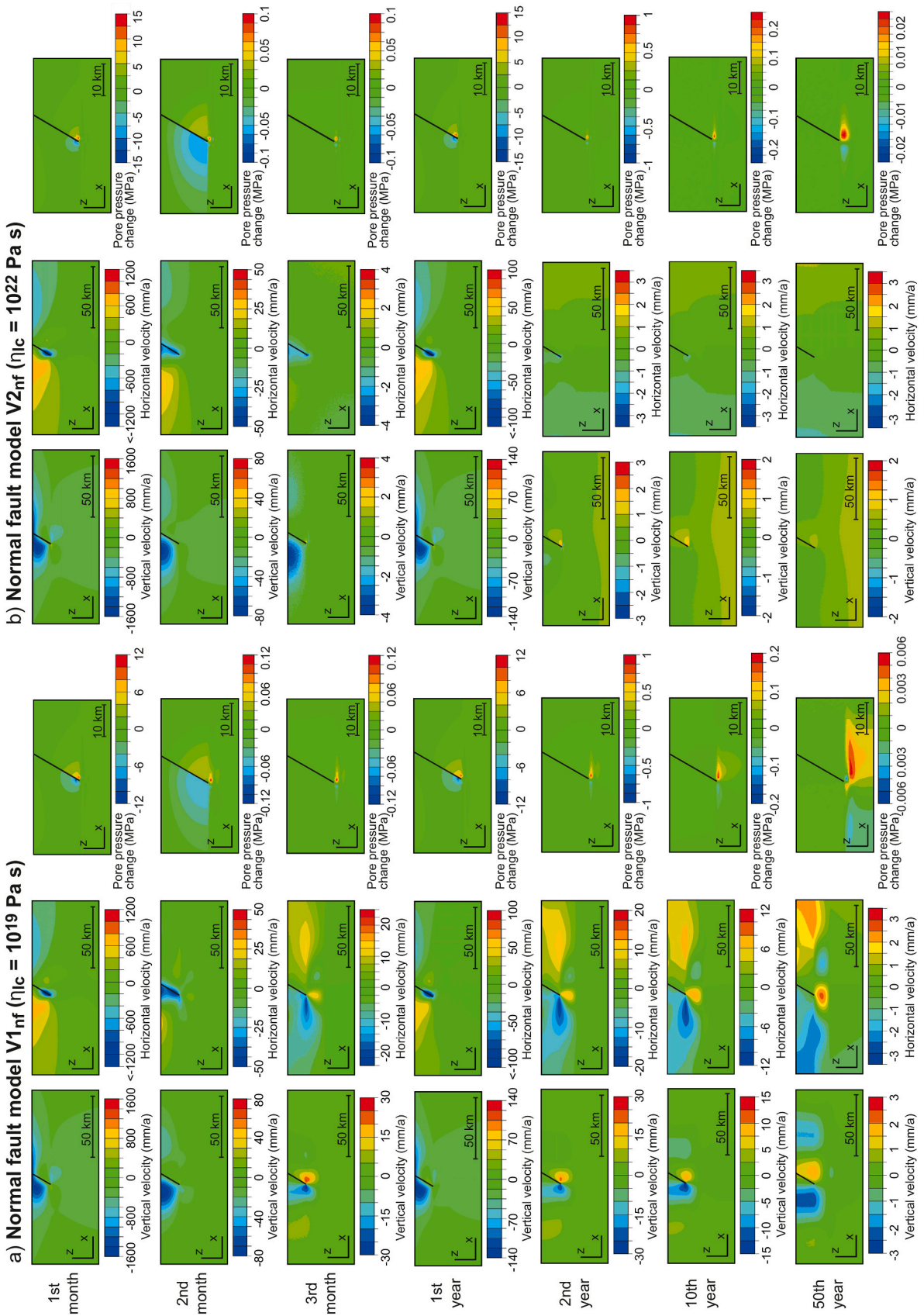
Fig. 8. Postseismic velocity fields and pore pressure changes from normal fault models (a) V1$_{nf}$ with a lower-crustal viscosity of $\eta_{lc} = 10^{19}$ Pa s and (b) V2$_{nf}$ with a lower-crustal viscosity of $\eta_{lc} = 10^{22}$ Pa s. No vertical exaggeration. Note that the velocity fields and pore pressure changes at all time points are averaged over the respective time interval, i.e. the velocity field and pore pressure change for the first postseismic year is integrated over the time period between the beginning and the end of the first year after the earthquake.

In the models with a viscosity of 10^{22} Pa s in the lower crust (V2$_{nf}$, V2$_{tf}$), high velocity perturbations similar to the reference model R1$_{nf}$ and R1$_{tf}$ occur until the second month after the earthquake (Fig. 8b, S5b). In the third month, the largest velocity perturbations can be found in the hanging wall of both normal and thrust fault (V2$_{nf}$, V2$_{tf}$), similar to the third month of the reference model without viscoelastic relaxation (R2$_{nf}$, R2$_{tf}$). From the sixth month onwards and in the following years, the velocities decrease and the velocity fields slowly transition to the patterns induced by the regional deformation with weak perturbations occurring around the fault tip and at the transition between upper and lower crust up to 150 km away from the fault. The pore pressure changes in the first month reach ±15 MPa (normal fault model V2$_{nf}$) and ±12 MPa (thrust fault model V2$_{tf}$). Until the 50th model year, the pore pressure distribution in both models evolves – with a slight temporal delay and a higher magnitude – similarly to the reference model R1$_{nf}$ and R1$_{tf}$.

In contrast to variations in the lower-crustal viscosity, varying the viscosity of the lithospheric mantle in our models (V3$_{nf}$, V3$_{tf}$: 10^{22} Pa s) does not have a large effect on the velocities and pore pressure distribution around the fault (Figs. S6). Both temporal evolution and spatial patterns of the velocity field and the pore pressure changes are similar to the reference model (R1$_{nf}$, R1$_{tf}$).

3.2.4. Endmember models with variable viscosity and permeability

Based on the model results described in sections 3.2.1–3.2.3, this section presents four endmember models, in which we combined a high/low permeability of the upper crust with a low/high viscosity of the lower crust to maximize or minimize the effects from the interaction between pore pressure changes and viscoelastic relaxation (Table 2, Figs. 9-10 and S7-S8).

In models PV1$_{nf}$ and PV1$_{tf}$ we combine a high permeability of 10^{-11} m^2 in the upper crust with a low viscosity of 10^{19} Pa s in the lower crust (Fig. 9a, S7a). In the first month after the earthquake, the results show the same velocity distributions as in the reference model R1$_{nf}$ and R1$_{tf}$, models P1$_{nf}$ and P1$_{tf}$ with the same permeability and models V1$_{nf}$ and V1$_{tf}$ with the same viscosity but the magnitudes of the velocities best agree with models P1$_{nf}$ and P1$_{tf}$. This also applies to the pore pressure changes in the first month. Already in the second month, the velocities strongly decrease. Hanging wall subsidence, footwall uplift and extension across the normal fault as well as hanging wall uplift and footwall subsidence and shortening across the thrust fault already start in the second month onwards. The velocity fields and also the pore pressure distributions now resemble the results obtained for third month of models V1$_{nf}$ and V1$_{tf}$. The further evolution of PV1$_{nf}$ and PV1$_{tf}$ is similar to models V1$_{nf}$ and V1$_{tf}$.

Models PV2$_{nf}$ and PV2$_{tf}$ have a low viscosity of 10^{19} Pa s combined with a low permeability of 10^{-17} m^2 (Fig. 9b, S7b). This parameter combination yields considerably lower velocities in the first month and velocity fields comparable to the third month of models V1$_{nf}$ and V1$_{tf}$. Like in models P4$_{nf}$ and P4$_{tf}$, no major changes occur in the velocity fields during the following months until the fifth year. Until the 50th year, models PV2$_{nf}$ and PV2$_{tf}$ show a similar evolution of the velocity distributions as V1$_{nf}$ and V1$_{tf}$, but with different magnitudes. The pore pressures develop comparable to models P4$_{nf}$ and P4$_{tf}$, with slightly higher pore pressure changes around the fault tip in the first months and year after the earthquake and pore pressure expansion over the following years.

The combination of a high permeability in the upper crust (10^{-11} m^2) and a high viscosity in the lower crust (10^{22} Pa s) in models PV3$_{nf}$ and PV3$_{tf}$ (Fig. 10a, S8a) leads to similar velocity fields in the first month, that occur in the reference models (R1$_{nf}$, R1$_{tf}$), the models with the same permeability (P1$_{nf}$, P1$_{tf}$) and viscosity structure (V2$_{nf}$, V2$_{tf}$). The pore pressure distributions are similar to models V2$_{nf}$ and V2$_{tf}$ for the first month and year after the earthquake. In the second month, velocities strongly decrease. While the patterns of the velocity fields are similar to models V2$_{nf}$ and V2$_{tf}$, their magnitudes are one order of magnitude

lower. The velocity patterns of the third month resemble the ones observed in the sixth month in models V2$_{nf}$ and V2$_{tf}$, with a similar evolution over the following years, i.e. the velocity fields are dominated by the regional deformation and only weakly perturbed around the fault. The pore pressure changes of the second month in models PV3$_{nf}$ and PV3$_{tf}$ are equivalent to the ones occurring in the third month in model V2$_{nf}$ and V2$_{tf}$. Afterwards, they develop similarly as in models V2$_{nf}$ and V2$_{tf}$.

Finally, models PV4$_{nf}$ and PV4$_{tf}$ combine a high viscosity (10^{22} Pa s) with a low permeability (10^{-17} m^2) (Fig. 10b, S8b). The results show the least pronounced perturbations in the velocities and pore pressure distributions of all models. During the first year, the velocity fields are mainly perturbed around the fault tip and at the surface near the fault, similar to models P4$_{nf}$ and P4$_{tf}$. Until the tenth year, the models PV4$_{nf}$ and PV4$_{tf}$ also show slight opposite movements in the horizontal direction. On both sides of the fault, subsidence occurs in the normal fault model and uplift in the thrust fault model until the 50th year. The velocity perturbations around the fault tip and at the surface slowly dissipate over the years, similar to models V2$_{nf}$ and V2$_{tf}$. The pore pressure evolution in models PV4$_{nf}$ and PV4$_{tf}$ is similar to model set P4$_{nf}$ and P4$_{tf}$ from the first month onwards, with the magnitudes of the pore pressure changes being slightly higher.

4. Discussion

Our parameter study reveals that both poroelastic effects and viscoelastic relaxation modify the postseismic pore pressure changes and velocities through space and time, depending on the permeability and viscosity, respectively. In the following, we discuss the main findings and limitations of our models and evaluate the relative importance of poroelastic effects and postseismic viscoelastic relaxation for the velocity and pore pressure distributions (Section 4.1). In Section 4.2, we qualitatively compare our findings with data and models from natural normal and thrust fault earthquakes. Note that the application of our models to data from specific earthquakes is beyond the scope of our study, because the main purpose of our study is advancing the general understanding of the underlying processes. Also, specific models including poroelastic and/or viscoelastic effects are already available for a number of earthquakes (e.g. Albano et al., 2017, 2019, 2021; Freed and Lin, 2001; Luo and Liu, 2010; Masterlark and Wang, 2002; Nespoli et al., 2018; Ryder et al., 2007, 2010; Tung and Masterlark, 2018).

4.1. Discussion of model results, model limitations and implications for the relative importance of viscoelastic relaxation and poroelastic effects

During the coseismic phase, the sudden slip on the model fault causes crustal movements typical of normal and thrust fault earthquakes, i.e. hanging wall subsidence and footwall uplift in the normal fault model and hanging wall uplift and footwall subsidence in the thrust fault model (Fig. 2a, b). Horizontal movements in the footwall and hanging wall are directed away from the normal fault and toward the thrust fault (Fig. 2b, d). Compared to the analytical solutions by Okada (1985), the vertical displacements occur in broader zones on both sides of the fault whereas the horizontal displacements are largely similar (Fig. 2b, d). The differences between the displacements can be attributed to the fact that Okada (1985) simplifies the crust as an isotropic, homogeneous elastic half-space, whereas our models account for gravity, isostatic effects, rheological layering of the lithosphere and poroelastic effects. Furthermore, Okada (1985) assumes a constant amount of slip on a rectangular fault plane, whereas the slip distribution in our finite-element models is tapered, i.e. it goes to zero at the lower fault tip. As shown by previous studies, the consideration of tapered fault slip, isostatic effects and/or rheological layering in finite-element models leads to more realistic surface displacements in agreement with geodetically measured surface displacement patterns (e.g. Hampel and Hetzel, 2015; Hsu et al., 2011; Tung et al., 2018b).
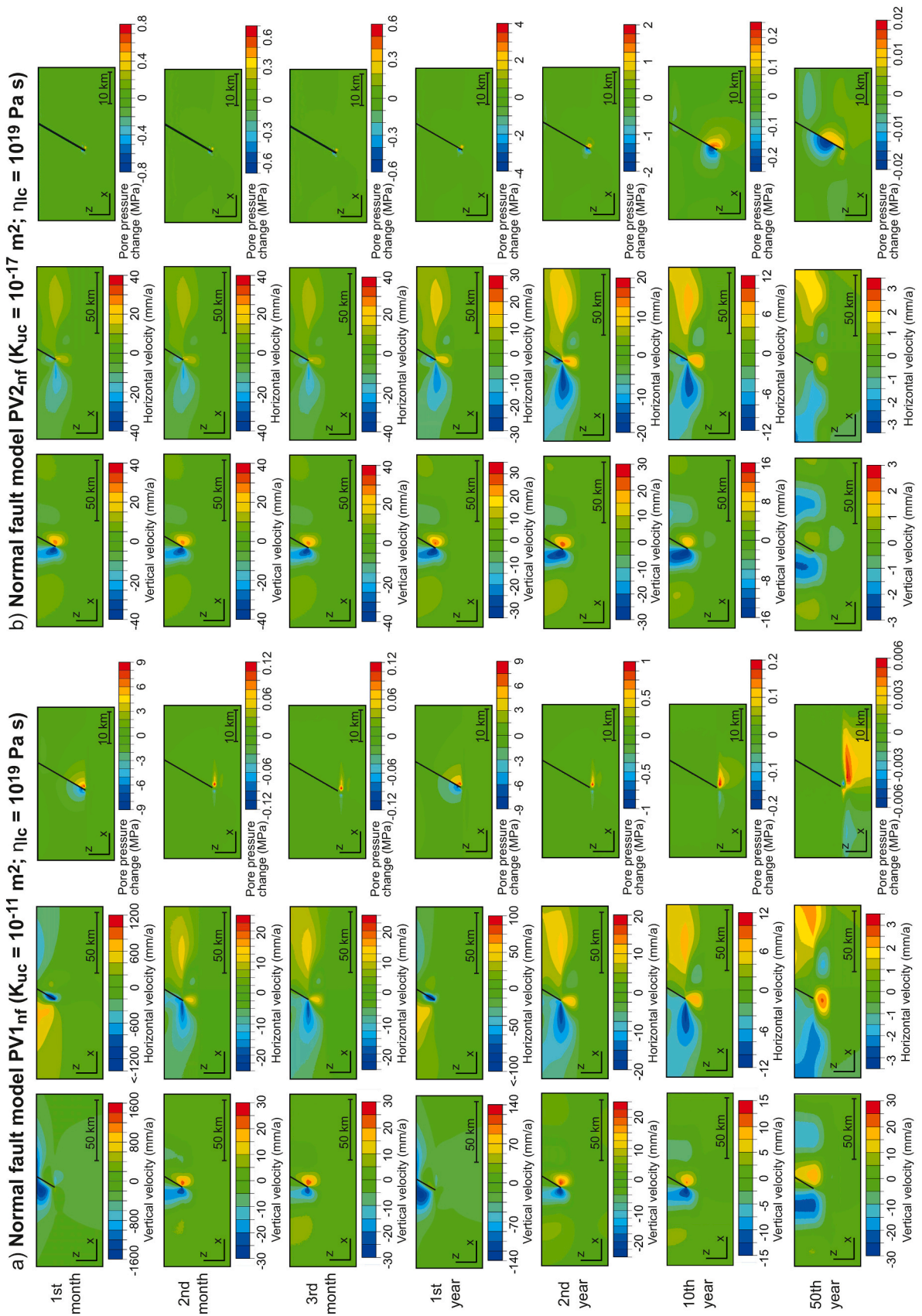
Fig. 9. Postseismic velocity fields and pore pressure changes from normal fault models (a) PV1$_{nf}$ with an upper-crustal permeability of K$_{uc}$ = 10^{-11} m^2 and a lower-crustal viscosity of η$_{lc}$ = 10^{19} Pa s and (b) PV2$_{nf}$ with an upper-crustal permeability of K$_{uc}$ = 10^{-17} m^2 and a lower-crustal viscosity of η$_{lc}$ = 10^{19} Pa s. No vertical exaggeration. Note that the velocity fields and pore pressure changes at all time points are averaged over the respective time interval, i.e. the velocity field and pore pressure change for the first postseismic year is integrated over the time period between the beginning and the end of the first year after the earthquake.
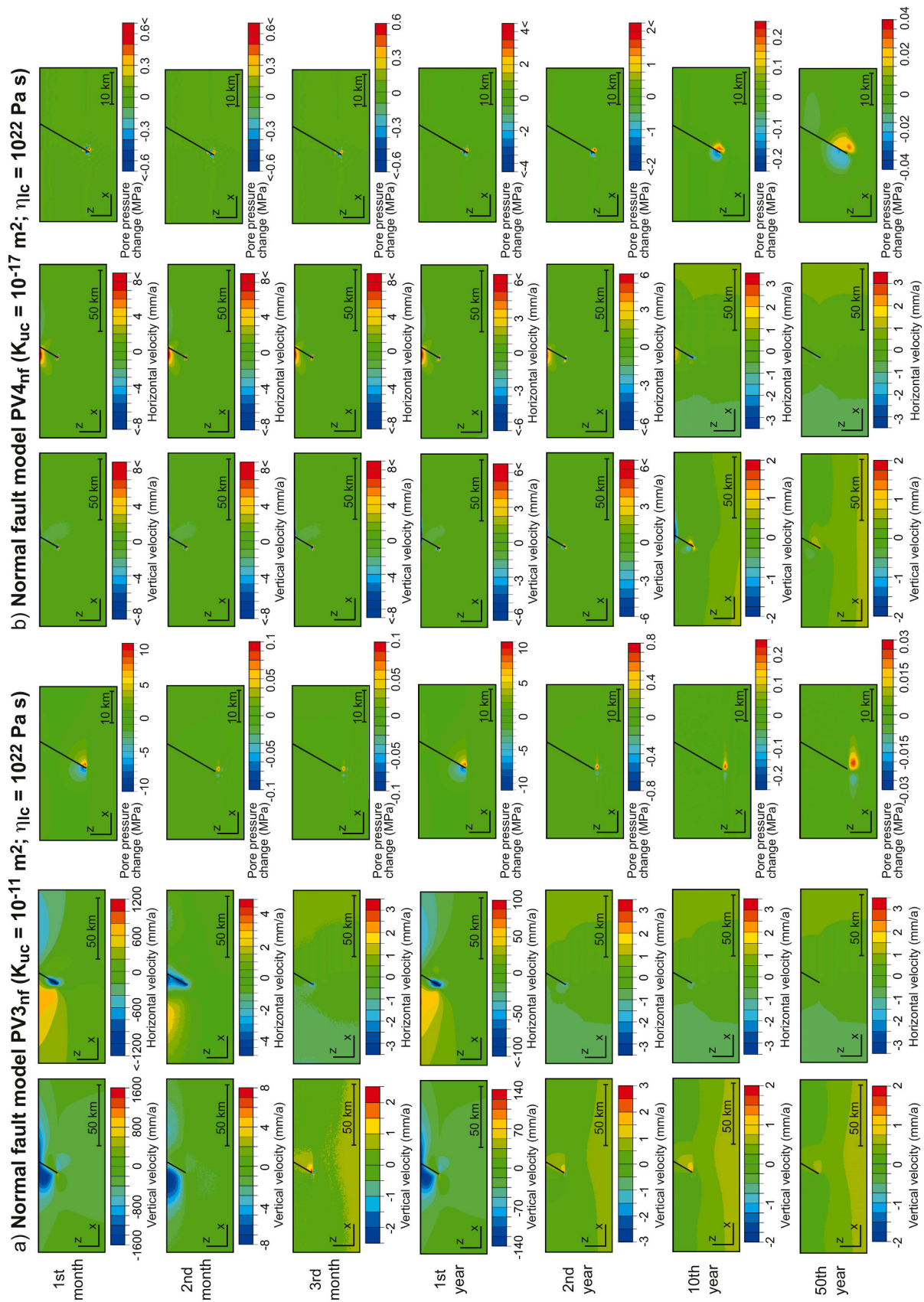
Fig. 10. Postseismic velocity fields and pore pressure changes from normal fault models (a) PV3$_{nf}$ with an upper-crustal permeability of K$_{uc}$ = 10^{-11} m2 and a lower-crustal viscosity of η$_{lc}$ = 10^{22} Pa s and (b) PV4$_{nf}$ with an upper-crustal permeability of K$_{uc}$ = 10^{-17} m2 and a lower-crustal viscosity of η$_{lc}$ = 10^{22} Pa s. No vertical exaggeration. Note that the velocity fields and pore pressure changes at all time points are averaged over the respective time interval, i.e. the velocity field and pore pressure change for the first postseismic year is integrated over the time period between the beginning and the end of the first year after the earthquake.

With respect to the strain regime, the coseismic horizontal displacements indicate extension across the normal fault and to shortening across the thrust fault (Fig. 2). In the footwall and hanging wall, however, shortening prevails in the normal fault model and extension in the thrust fault model (Fig. 2e). The phenomenon of coseismic shortening in the footwall of normal faults and of coseismic extension in the hanging wall of thrust faults is well known from geological field observations from natural earthquakes (e.g. Crone et al., 1987; King and Vita-Finzi, 1981; Lin et al., 2009; Liu-Zeng et al., 2009; Meghraoui et al., 1988; Myers and Hamilton, 1964; Philip and Meghraoui, 1983; Slemmons, 1957; Yu et al., 2010). As shown in a previous numerical modelling study (Hampel and Hetzel, 2015), the coseismic strain patterns are also recognizable in GPS data from intra-continental dip-slip faults (e.g. Cheloni et al., 2010; Chen et al., 2006; Serpelloni et al., 2012; Yu et al., 2001). During the postseismic phase, the coseismically induced strain fields are gradually altered by the combined effect of viscoelastic flow and interseismic strain accumulation (Hampel and Hetzel, 2015). Again, the spatiotemporal evolution of the strain field is also visible in GPS data (e.g. Cheloni et al., 2010; Yu et al., 2003).

In contrast to the coseismic vertical displacements, the vertical movements during the early postseismic phase depends on whether poroelastic effects are considered in the respective experiment. Models including poroelastic effects (e.g. $R1_{nf}$, $R1_{tf}$ and $R2_{nf}$, $R2_{tf}$) reveal that the footwall and hanging wall move in the same vertical direction, i.e. both experience subsidence in the normal fault model and uplift in the thrust fault model, respectively (Figs. 3, 4). In contrast, models including only viscoelastic relaxation but no fluid flow ($R3_{nf}$, $R3_{tf}$) do not show this pattern (Figs. 3c, 4c). This implies that vertical movements are caused by the poroelastic effects, i.e. they are driven by pore fluid diffusion and depend on the permeability. The dependence of the vertical movements near the fault on the presence or absence of pore fluid flow in a numerical model is supported by a comparison with models that either considered (e.g. Albano et al., 2017, 2019, 2021) or neglected pore fluid flow (e.g. Barbot and Fialko, 2010; Hampel and Hetzel, 2015; Pollitz, 1997). To further evaluate if the postseismic vertical movements of hanging wall and footwall in the same direction are indeed indicative of poroelastic effects, detailed geodetic data from both fault-bounding blocks at different time intervals after the earthquake would be desirable. So far, the available geodetic data from intra-continental earthquakes do not yield a consistent picture, partly because of the larger uncertainty involved with measurements of vertical movements. For example, 60 days after the 2009 L'Aquila normal fault earthquake, the 8 GPS stations on the hanging wall of the Paganica fault show subsidence of up to 50 mm while the one station located on the footwall showed 5.4 mm of uplift (Cheloni et al., 2010). In contrast, the postseismic deformation field of the 2016 Amatrice-Norcia earthquakes was characterized by primarily subsidence of the hanging wall but subsidence and uplift in the footwall (Mandler et al., 2021). After the 2003 Chengkung (Taiwan) thrust fault earthquake, the 3 GPS stations located near the fault surface trace recorded uplift (Chen et al., 2006).

The further spatio-temporal evolution of the postseismic velocity field depends on the permeability of the crust. Models with upper-crustal permeabilities higher than 10^{-15} m^2 show elevated vertical and horizontal velocities and strong velocity perturbations in the first month after the earthquake, which decrease rapidly in the following few months. The velocities are highest in a small area around the fault of up to 20 km away from the fault. For lower permeabilities, the velocities in the first month show lower initial values but a slower decrease over time. Note that, although both vertical and horizontal velocities generally decrease over time, the specific velocity values and patterns depend on the time interval over which the velocities are integrated. In Figs. 3-10 and S1-S8, we illustrate this by showing the velocities for the first months and integrated over the first year after the earthquake. If the velocities are integrated over a month, the highest velocities occur during the first month but generally decrease until the sixth month after the earthquake. If the velocity field integrates over the entire first year

after the earthquake, elevated values are obtained and the velocity pattern of the first year generally resembles the one of the first month. This indicates that a velocity field integrated over the first postseismic year may be dominated by the signal from poroelastic effects rather than by the signal from incipient viscoelastic relaxation (see Section 4.2 for a discussion of the relative importance of the two processes). Caution is therefore advised when choosing the time interval for analysing postseismic velocity fields obtained, for example, from geodetic data. Sometimes, postseismic velocity fields integrated over the early postseismic phase are interpreted to reflect the signal from incipient viscoelastic relaxation, under the assumption that poroelastic effects have largely disappeared (e.g. Aoudia et al., 2003; Liu-Zeng et al., 2020; Mandler et al., 2021), which may not always be the case.

The return to velocity patterns typical of normal and thrust faults occurs within the first few months in models $P1_{nf}$ and $P1_{tf}$ and $R1_{nf}$ and $R1_{tf}$ and in the second and after the fifth year in models $P2_{nf}$ and $P2_{tf}$ and $P3_{nf}$ and $P3_{tf}$, respectively. For lower permeabilities (e.g. model $P4_{nf}$, $P4_{tf}$), the unusual movements are only slightly recognizable. Models $R2_{nf}$ and $R2_{tf}$, which considers poroelastic effects but no viscoelastic relaxation shows the same velocity evolution in the first two months after the earthquake as the reference models $R1_{nf}$ and $R1_{tf}$. In the third month, the velocity fields are still disturbed, and in the following months and years, only the regional velocity fields largely remain, without significant velocity perturbations. Hence, models $R2_{nf}$ and $R2_{tf}$ show that in absence of postseismic viscoelastic relaxation, poroelastic effects seem to affect the velocity fields until the third month.

With respect to the pore pressure distribution, we observe in all models that the areas with maximum and minimum pore pressure changes are mostly located within a few kilometres around the fault tip. Relative to the coseismic phase, the postseismic pore pressure changes are inverted. Because of the higher magnitude, this dominant pattern of pore pressure changes in our models overprints the pore pressure changes with alternating zones of negative and positive pore pressure changes that may be expected from a double-couple earthquake source function with conjugate zones of extension and shortening. The alternating zones of negative and positive pore pressure changes can be made visible by limiting the colour scale to a narrower range of values (Supplementary Fig. S9; Zhou and Burbey, 2014). As noted by previous studies, deformation patterns may differ from the theoretically expected conjugate pattern if, for example, anisotropy, pore pressure and the background stress state are considered (e.g. Foulger and Julian, 2015; Hamiel et al., 2005; Vavrycuk, 2005; Wang, 1997). Notably, non-double-couple components in seismic moment tensors have been reported for natural and induced earthquakes and related, for example, to anisotropies, pore pressure and/or stress state (e.g. Frohlich, 1994; Martinez-Garzon et al., 2017; Miller et al., 1998).

The pore pressure changes normalize during the postseismic phase at different rates and slowly migrate into the lower crust over the years. Models $P1_{nf}$ and $P1_{tf}$ and $P2_{nf}$ and $P2_{tf}$ with high permeabilities in the upper crust ($K_{uc} = 10^{-11}$ m^2 and $K_{uc} = 10^{-13}$ m^2) show pore pressure changes of the same magnitude as the pore pressure changes of the coseismic phase of the reference models $R1_{nf}$ and $R1_{tf}$, followed by pore pressure migration into the lower crust with only low magnitude, i.e. hydrostatic conditions are reached already in the first month (Fig. 6a, b, S1a and S1b). With decreasing permeability in the upper crust (lower than $K_{uc} = 10^{-13}$ m^2), the magnitude of the pore pressure changes decreases in the first month, but remains higher in the following months and years, indicating that fluids diffuse slower within the upper crust, pore fluid pressure normalization lasts longer and hydrostatic conditions are therefore only reached after years or decades, respectively. In models $P4_{nf}$ and $P4_{tf}$ ($K_{uc} = 10^{-17}$ m^2, Figs. 7b and S2b), this slow fluid diffusion is particularly well illustrated over the entire 50-year period.

Fig. 11 shows the temporal evolution of the pore pressure in the overpressurized model area near the fault tip for different permeabilities in the upper crust. With respect to the temporal decrease of the pore pressure changes, we note that dissipation times in 2D finite-element
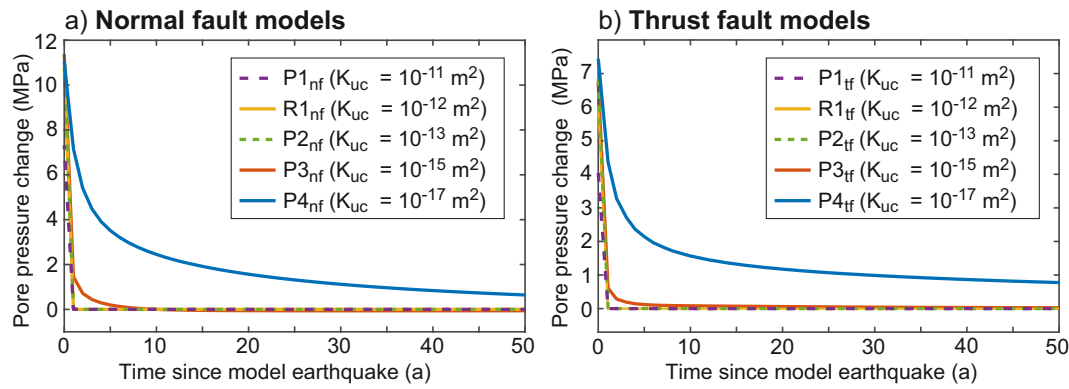
Fig. 11. Temporal evolution of the postseismic pore pressure changes in (a) normal fault and (b) thrust fault models.

models may somewhat differ from those in 3D models because the fluid flow is forced to occur in two dimensions only. A comparison between the 2D models presented in this study and the results from preliminary 3D models suggests that the difference in dissipation times effect may become recognizable for permeabilities lower than ca. 10^{-15} m^2. However, the observed difference in dissipation times in 2D and 3D models is small and does not affect our conclusions obtained from the 2D models regarding the timescale of the interaction of poroelastic effects with viscoelastic relaxation. In the reference models R1$_{nf}$ and R1$_{tf}$, the pore pressure changes decrease exponentially and reach largely hydrostatic conditions within four days. In models with permeabilities higher than 10^{-14} m^2, the pore pressure normalizes within the first year after the earthquake. For a permeability of $K_{uc} = 10^{-15}$ m^2 (models P3$_{nf}$, P3$_{tf}$), the pore pressure relaxation lasts ~10 years. In the models with a permeability of $K_{uc} = 10^{-17}$ m^2 (models P4$_{nf}$, P4$_{tf}$), the pore pressure relaxes very slowly, with the result that the hydrostatic pore pressure of the preseismic phase is still not fully recovered after 50 years. Thus, our results underline that the permeability of the upper crust has a strong effect on the pore fluid diffusion during the postseismic phase. The lower the permeability, the weaker is the fluid flow and the longer takes the pore pressure normalization. In contrast, the permeability of the lower crust has a negligible effect on the pore pressure evolution in the upper crust. However, an increase of the permeability in the lower crust may lead to an increased fluid flow into the lower crust.

In summary, a high permeability in the upper crust causes strong poroelastic effects with large pore pressure changes and velocity perturbations, but these effects last only for a few days to a few months after the earthquake. A low permeability in the upper crust leads to weak, but long-lasting poroelastic effects, which are still recognizable several years after the earthquake. Therefore, the poroelastic effects observed in our models act on timescales that overlap with the spatio-temporal evolution of the postseismic viscoelastic relaxation process. A change in the viscosity in the lower crust compared to the reference models may therefore affect the model results already for the early postseismic phase. For example, a viscosity of 10^{19} Pa s leads to larger velocity perturbations, which slightly change over the period of 50 years, mainly in an area of 10–20 km around the fault, but up to several tens of kilometres away from the fault (models V1$_{nf}$, V1$_{tf}$). The vertical and horizontal velocities are high in the first years after the earthquake and decrease over the following years. For a higher viscosity (models V3$_{nf}$, V3$_{tf}$; 10^{22} Pa s), only weak velocity perturbations with low velocities occur, which are recognizable several tens of kilometres away from the fault and only change negligibly over the decades. Hence, as can be expected, an increase of the viscosity in the lower crust leads to slower but more prolonged viscoelastic relaxation. As illustrated by the models R3$_{nf}$ and R3$_{tf}$, which considers viscoelastic relaxation but no pore fluid pressure (Fig. 3c and 4c), velocity perturbations occur from the first month onward, with only negligible changes over the next 50 years. This underlines that a signal from viscoelastic relaxation is already recognizable in the first month after the earthquake. In presence of pore fluid flow (models R1$_{nf}$, R1$_{tf}$ and R2$_{nf}$, R2$_{tf}$), however, the signal from viscoelastic relaxation is overprinted by the signal from the poroelastic effects, which strongly influence the velocity fields in the early postseismic phase if the permeability is sufficiently high. As soon as the poroelastic effects decay, the viscoelastic relaxation signal starts to dominate the velocity fields, which is the case already in the third month in models with high permeabilities (e.g. models PV1$_{nf}$, PV1$_{tf}$ and PV3$_{nf}$, Pv3$_{tf}$). Models with a low permeability and a low viscosity (PV2$_{nf}$, PV2$_{tf}$) highlight the possibility that viscoelastic relaxation may dominate the velocity fields with pronounced velocity perturbations already from the first month onwards because the poroelastic effects are weak. For the combination of a low permeability and a high viscosity, the signals from both effects are weak but long-lasting, with the result that they overlap over several decades and cause weak velocity perturbations (models PV4$_{nf}$, PV4$_{tf}$).

4.2. Comparison with data and models for natural intra-continental earthquakes

A key region where a wealth of studies has investigated poroelastic effects after normal and thrust earthquakes with magnitudes of up to $M_w \sim 7$ are the Apennines and Emilia-Romagna region (Italy) (e.g. Albano et al., 2019, 2021; Antonioli et al., 2005; Chiarabba et al., 2009; Nespoli et al., 2018; Tung and Masterlark, 2018). In addition, a few studies used geodetic data from the postseismic phase to determine the rheological structure of the lithosphere beneath the Apennines and found low viscosities (~10^{18} Pa s) for the lower crust (Aoudia et al., 2003; Riva et al., 2007). Based on our model results, we would therefore expect an interaction between poroelastic effects and viscoelastic relaxation during the postseismic phase. Most studies, however, focussed on a specific time interval after the earthquake and therefore neglected either viscoelastic relaxation (e.g. Albano et al., 2017, 2019, 2021; Chiarabba et al., 2009; Nespoli et al., 2018) or poroelastic effects (Aoudia et al., 2003; Riva et al., 2007). In the following, we evaluate the results from the previous studies on earthquakes in the Apennines and Emilia-Romagna region in the light of our model results.

Poroelastic effects were studied, for example, by Albano et al. (2017, 2019, 2021) for the 2009 L'Aquila, 2012 Emilia-Romagna and the 2016 Amatrice-Visso-Norcia seismic sequences. Their finite-element models were either based on a simplified cross-section (Albano et al., 2019, 2021) or adjusted to the respective region (Albano et al., 2017) and used permeabilities between 10^{-12} and 10^{-17} m^2. Similar to our results, their findings indicate that the coseismic pore pressure changes are completely dissipated by fluid diffusion in the postseismic phase. Hydrostatic conditions are reached within a few days to up to one year, depending on the permeability in the crust. Compared to these results, our models indicate even longer pore pressure dissipation times of several years if the upper crust has a permeability of 10^{-17} m^2. Notably,

Albano et al. (2017, 2019, 2021) obtain postseismic surface subsidence for the 2009 L'Aquila and 2016 Amatrice-Visso-Norcia normal fault earthquakes and uplift for the 2012 Emilia-Romagna thrust fault earthquakes, which agrees well with our model results obtained for an idealized fault geometry. In addition, our models show that these unusual surface displacements are largest in the first year after the earthquake in models with high permeabilities.

The spatial distribution and dissipation time of the fluid overpressure is closely related to the spatio-temporal distribution of aftershocks. Seismological data from the 1997 Umbria-Marche earthquake sequence revealed that most of the main shocks and aftershocks occurred in areas where the pore pressure increased around the fault (Antonioli et al., 2005; Chiarabba et al., 2009). For the 2016 Amatrice-Visso-Norcia earthquakes, Albano et al. (2019) showed that the 26 October 2016 earthquake occurred when the fluid overpressure induced by the 24 August 2016 Amatrice earthquake had not yet dissipated. Overpressurization and pore pressure dissipation may trigger aftershocks, with the stress increase being related to the pore pressure dissipation time and hence to the permeability. In accordance with Albano et al. (2019)'s findings, our models indicate that the pore pressure may not fully dissipate within a few months after the earthquake if the permeability is lower than 10^{-13} m^2. For the crust beneath the Apennines, a permeability of 10^{-16} m^2 was derived by Tung and Masterlark (2018), who carried out modelling and Coulomb stress change calculations for the 2016 Amatrice-Visso-Norcia earthquakes. For such a permeability value, our model results indicate pore fluid dissipation times of more than a few months after the earthquake. With respect to the relative importance of poroelastic effects and viscoelastic relaxation for aftershock triggering, Tung and Masterlark (2018) argued that the postseismic Coulomb stress changes are dominated by poroelastic effects and that the contribution from viscoelastic relaxation is negligible. However, their model only considered viscoelastic behaviour in the mantle but not the low viscosity of the lower crust that was reported by Aoudia et al. (2003) and Riva et al. (2007).

Our model results support the notion that poroelastic effects dominate the velocity field during the early postseismic phase, i.e. when the probability of strong aftershocks is high. However, our findings indicate that the velocity field may also contain a signal from viscoelastic relaxation for sufficiently low viscosities of the lower crust (Figs. 8a, 9, S5a, S7). This is in accordance with the findings by Riva et al. (2007), who analysed the postseismic deformation after the 1997 Umbria-Marche earthquake sequence based on campaign GPS data from the time period between 1999 and 2003. Based on forward modelling, Riva et al. (2007) found that the observed postseismic deformation requires a contribution of viscoelastic relaxation. Their preferred model included a viscosity of $\sim10^{18}$ Pa s for the lower crust. In additional models, Riva et al. (2007) also evaluated a possible contribution by poroelastic effects, which they found to be small for the time period covered by the GPS data. Therefore, they disregarded poroelastic effects in their final forward models of the GPS data. Our model results agree with Riva et al. (2007)'s observation that poroelastic effects decrease within 2–3 years after the earthquake, however, poroelastic effects should not be neglected completely because for the observed permeability and viscosity values poroelastic and viscoelastic effects may overlap for years after an earthquake in the Apennines.

Compared to Italy, data on coseismically triggered poroelastic and viscoelastic effects are relatively sparse for other region with intracontinental dip-slip earthquakes. In Taiwan, for example, the 1999 Chi-Chi thrust fault earthquake triggered fluid flow and considerable changes in groundwater levels and river discharges (Lai et al., 2004; Wang et al., 2001, 2004). For the postseismic deformation field, however, poroelastic effects apparently did not play a major role (e.g. Hsu et al., 2007; Rousset et al., 2012; Zhu and Cai, 2009). Instead, the postseismic deformation field was largely dominated by viscoelastic relaxation due the presence of layers with low viscosities in the lithosphere (Rousset et al., 2012; Zhu and Cai, 2009). Based on inversion of

GPS data, Zhu and Cai (2009) derived viscosities of the lower crust and the upper mantle of 2.7×10^{18} and 4.2×10^{20} Pa s, respectively, while Rousset et al. (2012) obtained viscosities of 5×10^{17} and $0.5–1 \times 10^{19}$ Pa s at mid-crustal and lower crustal levels. As our models indicate, the absence of a major poroelastic signal in the early postseismic deformation field may be related to a low permeability in the upper crust, in particular when combined with low lower-crustal viscosities (Fig. S7). This may apply to Taiwan where a permeability of ca. 4×10^{-15} m^2 at a crustal depth of 10–20 km was derived from a seismological analysis of aftershocks and fluid migration after the 2016 Meinong earthquake (Hsu et al., 2020). Even lower permeabilities (10^{-16} to 10^{-18} m^2) were obtained from drill core samples of the host rock of the Chelungpu fault (Doan et al., 2006; Scibek, 2020). Taiwan may therefore provide an example of a region with thrust fault earthquakes where the timescales of poroelastic and viscoelastic effects overlap in a way that the resulting postseismic deformation is dominated by viscoelastic relaxation.

5. Conclusions

Based on two-dimensional finite-element models, we investigated the relative importance of poroelastic effects and postseismic viscoelastic relaxation during the earthquake cycle of intracontinental dip-slip faults and evaluated the results in terms of co- and postseismic pore pressure changes as well as vertical and horizontal velocities. Our experiments with variable permeabilities in the crust and variable viscosities in the lower crust or lithospheric mantle demonstrate that the earthquake induces pore fluid pressure changes especially around the fault tip, which dissipate by fluid diffusion within a few days to decades, depending on the permeability of the crust. These poroelastic effects dominate in the first few months, but still affect the velocity field years after the earthquake if the permeability of the upper crust is sufficiently low. Viscoelastic relaxation already occurs in the early postseismic phase, dominates the velocity field from about the second postseismic year onward and persists for several decades. Viscoelastic relaxation acts on spatial scales of up to several tens of kilometres away from the fault, whereas poroelastic effects occur mainly within 10–20 km around the fault. Our results show that poroelastic effects and postseismic viscoelastic relaxation may overlap in the early postseismic phase for up to several years, depending primarily on the combination of upper-crustal permeability and lower-crustal viscosity. Therefore, both processes should be considered when analysing geodetic data on postseismic surface deformation or calculating postseismic Coulomb stress changes. In future investigations, we will use 3D numerical models that will include fault arrays as well as poroelastic effects and viscoelastic relaxation to evaluate the combined effect of both processes on Coulomb stress changes.

CRediT authorship contribution statement

Jill Peikert: Conceptualization, Writing – original draft, Investigation, Visualization, Writing – review & editing. **Andrea Hampel:** Conceptualization, Writing – review & editing, Funding acquisition, Data curation. **Meike Bagge:** Writing – review & editing.

Declaration of Competing Interest

The authors declare that they have no known competing financial interests or personal relationships that could have appeared to influence the work reported in this paper.

Acknowledgements

Appendix A. Supplementary data

Supplementary data to this article can be found online at https://doi.org/10.1016/j.tecto.2022.229477.

References

ABAQUS Documentation, 2018. Dassault Systémes Simulia Corp.

Albano, M., Barba, S., Solaro, G., Pepe, A., Bignami, C., Moro, M., Saroli, M., Stramondo, S., 2017. Aftershocks, groundwater changes and postseismic ground displacements related to pore pressure gradients: Insights from the 2012 Emilia-Romagna earthquake. J. Geophys. Res. 122, 5622–5638. https://doi.org/10.1002/2017JB014009.

Albano, M., Barba, S., Saroli, M., Polcari, M., Bignami, C., Moro, M., Stramondo, S., Di Bucci, D., 2019. Aftershock rate and pore fluid diffusion: Insights from the Amatrice Visso-Norcia (Italy) 2016 seismic sequence. J. Geophys. Res. 124, 995–1015. https://doi.org/10.1029/2018JB015677.

Albano, M., Barba, S., Bignami, C., Carminati, E., Doglioni, C., Moro, M., Saroli, M., Samsonov, S., Stramondo, S., 2021. Numerical analysis of interseismic, coseismic and post-seismic phases for normal and reverse faulting earthquakes in Italy. Geophys. J. Int. 225, 627–645. https://doi.org/10.1093/gji/ggaa608.

Antonioli, A., Piccinini, D., Chiaraluce, L., Cocco, M., 2005. Fluid flow and seismicity pattern: evidence from the 1997 Umbria Marche (central Italy) seismic sequence. Geophys. Res. Lett. 32, L10311. https://doi.org/10.1029/2004GL022256.

Aoudia, A., Borghi, A., Riva, R., Barzaghi, R., Ambrosius, B.A.C., Sabadini, R., Vermeersen, L.L.A., Panza, G.F., 2003. Postseismic deformation following the 1997 Umbria-Marche (Italy) moderate normal faulting earthquakes. Geophys. Res. Lett. 30 (7), 1390. https://doi.org/10.1029/2002GL016339.

Bagge, M., Hampel, A., 2016. Three-dimensional finite-element modelling of coseismic Coulomb stress changes on intra-continental dip-slip faults. Tectonophysics 684, 52–62. https://doi.org/10.1016/j.tecto.2015.10.006.

Bagge, M., Hampel, A., 2017. Postseismic Coulomb stress changes on intra-continental dip-slip faults due to viscoelastic relaxation in the lower crust and lithospheric mantle: insights from 3D finite-element modelling. Int. J. Earth Sci. 106, 2895–2914. https://doi.org/10.1007/s00531-017-1467-8.

Barbot, S., Fialko, Y., 2010. A unified continuum representation of post-seismic relaxation mechanisms: semi-analytic models of afterslip, poroelastic rebound and viscoelastic flow. Geophys. J. Int. 182, 1124–1140. https://doi.org/10.1111/j.1365-246X.2010.04678.x.

Beauducel, F., . Okada: Surface deformation due to a finite rectangular source. https://www.mathworks.com/matlabcentral/fileexchange/25982-okada-surface-deformation-due-to-a-finite-rectangular-source. In: MATLAB Central File Exchange. Retrieved April 5, 2022.

Biot, M.A., 1941. General theory of three-dimensional consolidation. J. Appl. Phys. 12 (2), 155–164. https://doi.org/10.1063/1.1712886.

Burov, E.B., Watts, A.B., 2006. The long-term strength of continental lithosphere: "jelly sandwich" or "crème brûlée"? GSA Today 16 (1), 4–10. https://doi.org/10.1130/1052-5173(2006)016<4:tltSOc>2.0.cO;2.

Cheloni, D., D'Agostino, N., D'Anastasio, E., Avallone, A., Mantenuto, S., Giuliani, R., Mattone, M., Calcaterra, S., Gambino, P., Dominici, D., Radicioni, F., Fastellini, G., 2010. Coseismic and initial post-seismic slip of the 2009 M_w 6.3 L'Aquila earthquake, Italy, from GPS measurements. Geophys. J. Int. 181, 1539–1546. https://doi.org/10.1111/j.1365-246X.2010.04584.x.

Chen, H.-Y., Yu, S.-B., Kuo, L.-C., Liu, C.-C., 2006. Coseismic and postseismic surface displacements of the 10 December 2003 (Mw 6.5) Chengkung, eastern Taiwan, earthquake. Earth Planet Space 58, 5–21. https://doi.org/10.1186/BF03351908.

Chen, W.-P., Molnar, P., 1983. Focal depths of intracontinental and intraplate earthquakes and their implications for the thermal and mechanical properties of the lithosphere. J. Geophys. Res. 88, 4183–4214. https://doi.org/10.1029/JB088iB05p04183.

Chiarabba, C., De Gori, P., Boschi, E., 2009. Pore-pressure migration along a normal-fault system resolved by time-repeated seismic tomography. Geology 37 (1), 67–70. https://doi.org/10.1130/G25220A.1.

Crone, A.J., Machette, M.N., Bonilla, M.G., Lienkaemper, J.J., Pierce, K.L., Scott, W.E., Bucknam, R.C., 1987. Surface faulting accompanying the Borah Peak earthquake and segmentation of the Lost River fault, central Idaho. Bull. Seismol. Soc. Am. 77, 739–770. https://doi.org/10.1785/BSSA0770030739.

Dempsey, D.E., Archer, R.A., Ellis, S.M., Rowland, J.V., 2013. Hydrological effects of dip-slip fault rupture on a hydrothermal plume. J. Geophys. Res. 118, 195–211. https://doi.org/10.1029/2012JB009395.

Doan, M.L., Brodsky, E.E., Kano, Y., Ma, K.F., 2006. In situ measurement of the hydraulic diffusivity of the active Chelungpu fault, Taiwan. Geophys. Res. Lett. 33, L16317. https://doi.org/10.1029/2006GL026889.

Ellis, S., Stöckhert, B., 2004. Elevated stresses and creep rates beneath the brittle-ductile transition caused by seismic faulting in the upper crust. J. Geophys. Res. 109, B05407. https://doi.org/10.1029/2003JB002744.

England, P.C., Walker, R.T., Fu, B., Floyd, M.A., 2013. A bound on the viscosity of the Tibetan crust from the horizontality of palaeolake shorelines. Earth Planet. Sci. Lett. 375, 44–56. https://doi.org/10.1016/j.epsl.2013.05.001.

Foulger, G.R., Julian, B.R., 2015. Non-double-couple earthquakes. Encycl. Earthq. Eng. https://doi.org/10.1007/978-3-642-36197-5_290-1.

Freed, A.M., Lin, J., 1998. Time-dependent changes in failure stress following thrust earthquakes. J. Geophys. Res. 103 (B10), 24393–24409. https://doi.org/10.1029/98JB01764.

Freed, A.M., Lin, J., 2001. Delayed triggering of the 1999 Hector Mine earthquake by viscoelastic stress transfer. Nature 411, 180–183. https://doi.org/10.1038/35075548.

Frohlich, C., 1994. Earthquakes with Non-Double-couple Mechanisms. Science 264, 804–809. https://doi.org/10.1126/science.264.5160.804.

Gourmelen, N., Amelung, F., 2005. Postseismic mantle relaxation in the central Nevada seismic belt. Science 310, 1473–1476. https://doi.org/10.1126/science.1119798.

Hamiel, Y., Lyakhovsky, V., Agnon, A., 2005. Rock dilation, nonlinear deformation, and pore pressure change under shear. Earth Planet. Sci. Lett. 237, 577–589. https://doi.org/10.1016/j.epsl.2005.06.028.

Hampel, A., Hetzel, R., 2012. Temporal variation in fault friction and its effects on the slip evolution of a thrust fault over several earthquake cycles. Terra Nova 24, 357–362. https://doi.org/10.1111/j.1365-3121.2012.01073.x.

Hampel, A., Hetzel, R., 2015. Horizontal surface velocity and strain patterns near thrust and normal faults during the earthquake cycle: the importance of viscoelastic relaxation in the lower crust and implications for interpreting geodetic data. Tectonics 34. https://doi.org/10.1002/2014TC003605.

Hampel, A., Karow, T., Maniatis, G., Hetzel, R., 2010. Slip rate variations on faults during glacial loading and postglacial unloading: Implications for the viscosity structure of the lithosphere. In: Pascal, C., Stewart, I.S., Vermeersen, B.L.A. (Eds.), Neotectonics, Seismicity and Stress in Glaciated Regions, vol. 167. J. Geol. Soc. London, pp. 385–399.

Hampel, A., Li, T., Maniatis, G., 2013. Contrasting strike-slip motions on thrust and normal faults: Implications for space-geodetic monitoring of surface deformation. Geology 41 (3), 299–302. https://doi.org/10.1130/G33927.1.

Hampel, A., Lüke, J., Krause, T., Hetzel, R., 2019. Finite-element modelling of glacial isostatic adjustment (GIA): use of elastic foundations at material boundaries versus the geometrically non-linear formulation. Comput. Geosci. 122, 1–14. https://doi.org/10.1016/j.cageo.2018.08.002.

Henriquet, M., Avouac, J.-P., Bills, B.G., 2019. Crustal rheology of southern Tibet constrained from lake-induced viscoelastic deformation. Earth Planet. Sci. Lett. 506, 308–322. https://doi.org/10.1016/j.epsl.2018.11.014.

Hsu, Y.-F., Huang, H.-H., Huang, M.-H., Tsai, V.C., Chuang, R.Y., Feng, K.-F., Lin, S.-H., 2020. Evidence for fluid migration during the 2016 Meinong, Taiwan, aftershock sequence. J. Geophys. Res. 125, e2020JB019994 https://doi.org/10.1029/2020JB019994.

Hsu, Y.-J., Segall, P., Yu, S.-B., Kuo, L.-C., Williams, C.A., 2007. Temporal and spatial variations of post-seismic deformation following the 1999 Chi-Chi, Taiwan earthquake. Geophys. J. Int. 169, 367–379. https://doi.org/10.1111/j.1365-246X.2006.03310.x.

Hsu, Y.-J., Simons, M., Williams, C., Casarotti, E., 2011. Three-dimensional FEM derived elastic Green's functions for the coseismic deformation of the 2005 Mw 8.7 Nias-Simeulue, Sumatra earthquake. Geochem. Geophys. Geosyst. 12, Q07013. https://doi.org/10.1029/2011GC003553.

Ingebritsen, S.E., Manning, C.E., 2010. Permeability of the continental crust: dynamic variations inferred from seismicity and metamorphism. Geofluids 10, 193–205. https://doi.org/10.1111/j.1468-8123.2010.00278.x.

Kaufmann, G., Amelung, F., 2000. Reservoir-induced deformation and continental rheology in vicinity of Lake Mead, Nevada. J. Geophys. Res. 105, 16341–16358. https://doi.org/10.1029/2000JB900079.

Kenner, S., Segall, P., 1999. Time-dependence of the stress shadowing effect and its relation to the structure of the lower crust. Geology 27 (2), 119–122. https://doi.org/10.1130/0091-7613(1999)027<0119:TDOTSS>2.3.CO;2.

King, G.C.P., Muir-Wood, R., 1994. The impact of earthquakes on fluids in the crust. Ann. Geofis. 37 (6), 1453–1460. https://doi.org/10.4401/ag-4147.

King, G.C.P., Vita-Finzi, C., 1981. Active folding in the Algerian earthquake of 10 October 1980. Nature 292, 22–26. https://doi.org/10.1038/292022a0.

Klemperer, S.L., 2006. Crustal flow in Tibet: geophysical evidence for the physical state of Tibetan lithosphere, and inferred patterns of active flow. Geol. Soc. London Spec. Publ. 268, 39–70. https://doi.org/10.1144/GSL.SP.2006.268.01.03.

Lai, W.-C., Koizumi, N., Matsumoto, N., Kitagawa, Y., Lin, C.-W., Shieh, C.-L., Lee, Y.-P., 2004. Effects of seismic ground motion and geological setting on the coseismic groundwater level changes caused by the 1999 Chi-Chi earthquake, Taiwan. Earth Planet Space 56, 873–880. https://doi.org/10.1186/BF03352534.

Lin, A., Ren, Z., Jia, D., Wu, X., 2009. Co-seismic thrusting rupture and slip distribution produced by the 2008 M_w 7.9 Wenchuan earthquake, China. Tectonophysics 471, 203–215. https://doi.org/10.1016/j.tecto.2009.02.014.

Liu-Zeng, J., Zhang, Z., Wen, L., Tapponnier, P., Sun, J., Xing, X., Hu, G., Xu, Q., Zeng, L., Ding, L., Ji, C., Hudnut, K.W., van der Woerd, J., 2009. Co-seismic ruptures of the 12 May 2008, M_s 8.0 Wenchuan earthquake, Sichuan: East–west crustal shortening on oblique, parallel thrusts along the eastern edge of Tibet. Earth Planet. Sci. Lett. 286, 355–370. https://doi.org/10.1016/j.epsl.2009.07.017.

Liu-Zeng, J., Zhang, Z., Rollins, C., Gualandi, A., Avouac, J.-P., Shi, H., Wang, P., Chen, W., Zhang, R., Zhang, P., Wang, W., Li, Y., Wang, T., Li, Z., 2020. Postseismic deformation following the 2015 M_w7.8 Gorkha (Nepal) earthquake: New GPS data, kinematic and dynamic models, and the roles of afterslip and viscoelastic relaxation. J. Geophys. Res. 125, e2020JB019852 https://doi.org/10.1029/2020JB019852.

Luo, G., Liu, M., 2010. Stress evolution and fault interactions before and after the 2008 Great Wenchuan earthquake. Tectonophysics 491, 127–140. https://doi.org/10.1016/j.tecto.2009.12.019.

Malagnini, L., Lucente, F.P., De Gori, P., Akinci, A., Munafo, I., 2012. Control of pore fluid pressure diffusion on fault failure mode: Insights from the 2009 L'Aquila seismic sequence. J. Geophys. Res. 117, B05302. https://doi.org/10.1029/2011JB008911.

Mandler, E., Pintori, F., Gualandi, A., Anderlini, L., Serpelloni, E., Belardinelli, M.E., 2021. Post-seismic deformation related to the 2016 Central Italy seismic sequence

from GPS displacement time-series. J. Geophys. Res. 126, e2021JB022200 https://doi.org/10.1029/2021JB022200.

Manning, C.E., Ingebritsen, S.E., 1999. Permeability of the continental crust: Implications of geothermal data and metamorphic systems. Rev. Geophys. 37 (1) https://doi.org/10.1029/1998RG900002.

Martinez-Garzon, P., Kwiatek, G., Bohnhoff, M., Dresen, G., 2017. Volumetric components in the earthquake source related to fluid injection and stress state. Geophys. Res. Lett. 44, 800–809. https://doi.org/10.1002/2016GL071963.

Masterlark, T., 2003. Finite element model predictions of static deformation from dislocation sources in a subduction zone: Sensitivities to homogeneous, isotropic, Poisson-solid, and half-space assumptions. J. Geophys. Res. 108, B11. https://doi.org/10.1029/2002JB002296.

Masterlark, T., Wang, H.F., 2002. Transient stress-coupling between the 1992 Landers and 1999 Hector Mine, California, earthquakes. Bull. Seismol. Soc. Am. 92 (4), 1470–1486. https://doi.org/10.1785/0120000905.

Meghraoui, M., Jaegy, R., Lammali, K., Albarède, F., 1988. Late Holocene earthquake sequences on the El Asnam (Algeria) thrust fault. Earth Planet. Sci. Lett. 90, 187–203. https://doi.org/10.1016/0012-821X(88)90100-8.

Miller, A.D., Foulger, G.R., Julian, B.R., 1998. Non-double-couple earthquakes: 2. Observations. Rev. Geophys. 36, 531–568. https://doi.org/10.1029/98RG00717.

Myers, W.B., Hamilton, W., 1964. Deformation accompanying the Hebgen Lake earthquake of August 17, 1959. U.S. Geol. Surv. Profess. Pap. 435-1, 55–98.

Nespoli, M., Belardinelli, M.E., Gualandi, A., Serpelloni, E., 2018. Poroelasticity and fluid flow modeling for the 2012 emilia-romagna earthquakes: hints from GPS and InSAR data. Geofluids 2018, 1–15. https://doi.org/10.1155/2018/4160570.

Nishimura, T., Thatcher, W., 2003. Rheology of the lithosphere inferred from postseismic uplift following the 1959 Hebgen Lake earthquake. J. Geophys. Res. 108 (B8) https://doi.org/10.1029/2002JB002191.

Nur, A., Booker, J.R., 1972. Aftershocks caused by pore fluid flow? Science 175, 885–887. https://doi.org/10.1126/science.175.4024.885.

Nur, A., Mavko, G., 1974. Post-seismic viscoelastic rebound. Science 183, 204–206. https://doi.org/10.1126/science.183.4121.20.

Okada, Y., 1985. Surface deformation due to shear and tensile faults in a half-space. Bull. Seismol. Soc. Am. 75, 1135–1154. https://doi.org/10.1785/BSSA0750041135.

Parsons, T., Stein, R.S., Simpson, R.W., Reasenberg, P.A., 1999. Stress sensitivity of fault seismicity: a comparison between limited-offset oblique and major strike-slip faults. J. Geophys. Res. 104 (B9), 20183–20202. https://doi.org/10.1029/1999JB900056.

Philip, H., Meghraoui, M., 1983. Structural analysis and interpretation of the surface deformation of the El Asnam earthquake of October 10, 1980. Tectonics 2, 17–49. https://doi.org/10.1029/TC002i001p00017.

Piombo, A., Martinelli, G., Dragoni, M., 2005. Post-seismic fluid flow and Coulomb stress changes in a poroelastic medium. Geophys. J. Int. 162, 507–515. https://doi.org/10.1111/j.1365-246X.2005.02673.x.

Pollitz, F., 1997. Gravitational viscoelastic postseismic relaxation on a layered spherical Earth. J. Geophys. Res. 102, 17921–17941. https://doi.org/10.1029/97JB01277.

Rice, J.R., Cleary, M.P., 1976. Some basic stress diffusion solutions for fluid- saturated elastic porous media with compressible constituents. Rev. Geophys. 14, 227–241. https://doi.org/10.1029/RG014i002p00227.

Riva, R.E.M., Borghi, A., Aoudia, A., Barzaghi, R., Sabadini, R., Panza, G.F., 2007. Viscoelastic relaxation and long-lasting after-slip following the 1997 Umbria-Marche (Central Italy) earthquakes. Geophys. J. Int. 169, 534–546. https://doi.org/10.1111/j.1365-246X.2007.03315.x.

Rousset, B., Barbot, S., Avouac, J.-P., Hsu, Y.-J., 2012. Postseismic deformation following the 1999 Chi-Chi earthquake, Taiwan: Implication for lower-crust rheology. J. Geophys. Res. 117, B12405. https://doi.org/10.1029/2012JB009571.

Rudnicki, J.W., 1986. Slip on an impermeable fault in a fluid-saturated rock mass. Geophys. Monogr. Ser. 37, 81–89. https://doi.org/10.1029/GM037p0081.

Ryder, I., Parsons, B., Wright, T.J., Funning, G.J., 2007. Post-seismic motion following the 1997 Manyi (Tibet) earthquake: InSAR observations and modelling. Geophys. J. Int. 169, 1009–1027. https://doi.org/10.1111/j.1365-246X.2006.03312.x.

Ryder, I., Bürgmann, R., Sun, J., 2010. Tandem afterslip on connected fault planes following the 2008 Nima-Gaize (Tibet) earthquake. J. Geophys. Res. 115, B03404. https://doi.org/10.1029/2009JB006423.

Ryder, I., Wang, H., Bie, L., Rietbrock, A., 2014. Geodetic imaging of late postseismic lower crustal flow in Tibet. Earth Planet. Sci. Lett. 404, 136–143. https://doi.org/10.1016/j.epsl.2014.07.026.

Scholz, C.H., 1987. Wear and gouge formation in brittle faulting. Geology 15 (6), 493–495. https://doi.org/10.1130/0091-7613(1987)15<493:WAGFIB>2.0.CO;2.

Scibek, J., 2020. Multidisciplinary database of permeability of fault zones and surrounding protolith rocks at world-wide sites. Sci. Data 7, 95. https://doi.org/10.1038/s41597-020-0435-5.

Serpelloni, E., Anderlini, L., Belardinelli, M.E., 2012. Fault geometry, coseismic-slip distribution and Coulomb stress change associated with the 2009 April 6, Mw 6.3, L'Aquila earthquake from inversion of GPS displacements. Geophys. J. Int. 188, 473–489. https://doi.org/10.1111/j.1365-246X.2011.05279.x.

Shi, X., Kirby, E., Furlong, K.P., Meng, K., Robinson, R., Wang, E., 2015. Crustal strength in central Tibet determined from Holocene shoreline deflection around Siling Co. Earth Planet. Sci. Lett. 423, 145–154. https://doi.org/10.1016/j.epsl.2015.05.002.

Sibson, R.H., 1994. Crustal stress, faulting and fluid flow. Geol. Soc. London Spec. Publ. 78 (1), 69–84. https://doi.org/10.1144/GSL.SP.1994.078.01.07.

Slemmons, D.B., 1957. Geological effects of the Dixie Valley-Fairview Peak, Nevada, earthquake of December 16, 1954. Bull. Seismol. Soc. Am. 47, 353–375. https://doi.org/10.1785/BSSA0470040353.

Stober, I., Bucher, K., 2015. Hydraulic and hydrochemical properties of deep sedimentary reservoirs of the Upper Rhine Graben, Europe. Geofluids 15, 464–482. https://doi.org/10.1111/gfl.12122.

Tung, S., Masterlark, T., 2018. Delayed poroelastic triggering of the 2016 October Visso earthquake by the August Amatrice earthquake, Italy. Geophys. Res. Lett. 45, 2221–2229. https://doi.org/10.1002/2017GL076453.

Tung, S., Masterlark, T., Dovovan, T., 2018a. Transient poroelastic stress coupling between the 2015 M7.8 Gorkha, Nepal earthquake and its M7.3 aftershock. Tectonophysics 733, 119–131. https://doi.org/10.1016/j.tecto.2018.02.003.

Tung, S., Masterlark, T., Lo, D.S.L., 2018b. Finite Element Models of Elastic Earthquake Deformation. In: Svalova, V. (Ed.), Earthquakes. - Forecast, Prognosis and Earthquake Resistant Construction. https://doi.org/10.5772/intechopen.76612. IntechOpen.

Vavrycuk, V., 2005. Focal mechanisms in anisotropic media. Geophys. J. I. 161, 334–346. https://doi.org/10.1111/j.1365-246X.2005.02585.x.

Wang, C.-Y., Cheng, L.-H., Chin, C.-V., Yu, S.-B., 2001. Coseismic hydrologic response of an alluvial fan to the 1999 Chi-Chi earthquake,Taiwan. Geology 29 (9), 831–834. https://doi.org/10.1130/0091-7613(2001)029<0831:CHROAA>2.0.CO;2.

Wang, C.-Y., Wang, C.-H., Manga, M., 2004. Coseismic release of water from mountains: evidence from the 1999 (Mw 7.5) Chi-Chi, Taiwan, earthquake. Geology 32 (9), 769–772. https://doi.org/10.1130/G20753.1.

Wang, H.F., 1997. Effects of deviatoric stress on undrained pore pressure response to fault slip. J. Geophys. Res. 102, 17943–17950. https://doi.org/10.1029/97JB01358.

Wells, D.L., Coppersmith, K.J., 1994. New empirical relationships among magnitude, rupture length, rupture width, rupture area, and surface displacement. Bull. Seismol. Soc. Am. 84 (4), 974–1002.

Yu, G., Xu, X., Klinger, Y., Diao, G., Chen, G., Feng, X., Li, C., Zhu, A., Yuan, R., Guo, T., Sun, X., Tan, X., An, Y., 2010. Fault-scarp features and cascading-rupture model for the Mw 7.9 Wenchuan earthquake, eastern Tibetan Plateau, China. Bull. Seismol. Soc. Am. 100, 2590–2614. https://doi.org/10.1785/0120090255.

Yu, S.-B., Kuo, L.-C., Hsu, Y.-J., Su, H.-H., Liu, C.-C., Hou, C.-S., Lee, J.-F., Lai, T.-C., Liu, C.-C., Liu, C.-L., Tseng, T.-F., Tsai, C.-S., Shin, T.-C., 2001. Preseismic deformation and coseismic displacements associated with the 1999 Chi-Chi, Taiwan, earthquake. Bull. Seismol. Soc. Am. 91, 995–1012. https://doi.org/10.1785/0120000722.

Yu, S.-B., Hsu, Y.-J., Kuo, L.-C., Chen, H.-Y., Liu, C.-C., 2003. GPS measurement of postseismic deformation following the 1999 Chi-Chi, Taiwan, earthquake. J. Geophys. Res. 108 (B11), 2520. https://doi.org/10.1029/2003JB002396.

Zhou, X., Burbey, T.J., 2014. Pore-pressure Response to Sudden Fault Slip for Three Typical Faulting Regimes. Bull. Seismol. Soc. Am. 104, 793–808. https://doi.org/10.1785/0120130139.

Zhu, S., Cai, Y., 2009. Dynamic mechanisms of the post-seismic deformation following large events: Case study of the 1999 Chi-Chi earthquake in Taiwan of China. Sci. China Ser. D-Earth Sci. 52 (11), 1813–1824. https://doi.org/10.1007/s11430-009-0144-6.